Monthly Notices of the Royal Astronomical Society

MNRAS **550**, 1–20 (2026)
Advance Access publication 2026 June 10

https://doi.org/10.1093/mnras/stag1104

Multiwavelength modelling of the luminous fast blue optical transient AT2024wpp

Conor M. B. Omand ,[1★] Nikhil Sarin ,[2,3] Gavin P. Lamb ,[1] Daniel A. Perley ,[1] Andrew Mummery,[4] Hamid Hamidani ,[5] Steve Schulze ,[6] Emma R. Beasor ,[1] Aleksandra Bochenek ,[1] Helena-Margaret S. Grabham,[1] Sorcha R. Kennelly ,[1] Nguyen M. Khang ,[1] Shiho Kobayashi ,[1] Genevieve Schroeder ,[7] William N. Stone ,[1] Cairns Turnbull [1] and Jacob Wise [1]

[1]*Astrophysics Research Institute, Liverpool John Moores University, Liverpool Science Park IC2, 146 Brownlow Hill, Liverpool L3 5R, UK,*
[2]*Kavli Institute for Cosmology, University of Cambridge, Madingley Road, Cambridge, CB3 0HA, UK*
[3]*Institute of Astronomy, University of Cambridge, Madingley Road, Cambridge, CB3 0HA, UK*
[4]*School of Natural Sciences, Institute for Advanced Study, 1 Einstein Drive, Princeton, NJ 08540, USA*
[5]*Astronomical Institute, Graduate School of Science, Tohoku University, Sendai 980-8578, Japan*
[6]*Center for Interdisciplinary Exploration and Research in Astrophysics (CIERA), Northwestern University, 1800 Sherman Ave., Evanston, IL 60201, USA*
[7]*Department of Astronomy, Cornell University, Ithaca, NY 14853, USA*

Accepted 2026 June 3. Received 2026 May 16; in original form 2026 January 8

ABSTRACT

Luminous fast blue optical transients (LFBOTs) are a growing class of enigmatic energetic transients. They show fast rises and declines, high temperatures throughout their evolution, and non-thermal emission in radio and X-rays. Their power source is currently unknown, but proposed models include engine-driven supernovae, interaction-powered supernovae, shock cooling emission, intermediate mass black hole tidal disruption events (IMBH TDEs), and Wolf–Rayet/black hole mergers, among others. AT2024wpp is the most optically luminous LFBOT to date and has been observed extensively at multiple wavelengths, including radio, optical, UV, and X-rays. We take models from multiple scenarios and fit them to the AT2024wpp optical, radio, and X-ray light curves to determine which of these scenarios can best describe all aspects of the data. We show that none of the multiwavelength light-curve models can reasonably explain the data, and that other physical arguments disfavour models with homologously expanding ejecta. We discuss how a stellar mass/IMBH TDE of a low-mass star can be tested with late-time observations, and what other scenarios could possibly explain the broad-band data.

Key words: transients: supernovae – transients: tidal disruption events – stars: black holes.

1 INTRODUCTION

Recent high-cadence wide-field surveys, such as the Zwicky Transient Facility (ZTF; E. C. Bellm et al. 2019a) and the Asteroid Terrestrial-impact Last Alert System (ATLAS; J. L. Tonry 2011; J. L. Tonry et al. 2018), have led to the discovery and characterization of several new types of fast optical transients (M. R. Drout et al. 2014; I. Arcavi et al. 2016; M. Pursiainen et al. 2018; A. Y. Q. Ho et al. 2023b). These transients evolve faster than typical supernovae (SNe) and can have peak luminosities similar to superluminous supernovae (SLSNe; A. Gal-Yam 2012; M. Nicholl 2021; S. Gomez et al. 2024). These properties rule out typical ^{56}Ni-powered core-collapse or thermonuclear SN models, since the mass of ^{56}Ni required to explain the luminosity would be larger than the mass of the ejected material. Further studies have shown that many of these transients are likely Type Ibn/Icn SNe (A. Y. Q. Ho et al. 2023b); SNe powered by the interaction between the ejected material and circumstellar material (CSM). However, a few of the more luminous fast optical transients have shown multi-component multiwavelength signatures consistent with a central engine (A. Y. Q. Ho et al. 2019; R. Margutti et al. 2019; A. Y. Q. Ho et al. 2020, 2022; B. D. Metzger 2022a; A. A. Chrimes et al. 2024b); these transients have become known as luminous fast blue optical transients (LFBOTs).

The prototype LFBOT is AT2018cow (‘the Cow’, S. J. Prentice et al. 2018), the closest observed event so far ($z = 0.014$). The optical emission rose to peak within ~ 2.5 d, and peaked at an absolute magnitude ~ -20.5. The optical spectra had only a few broad features, indicating expansion velocities $\gtrsim 0.1c$ and temperatures $\sim$30 000 K. Around 15 d, the spectrum began to show H and He features at velocities $\sim$3000–4000 km s^{-1}, but showed no evidence of cooling to normal late-time SN temperatures (R. Margutti et al. 2019; D. A. Perley et al. 2019; D. Xiang et al.

★ E-mail: c.m.omand@ljmu.ac.uk

© The Author(s) 2026.
Published by Oxford University Press on behalf of Royal Astronomical Society. This is an Open Access article distributed under the terms of the Creative Commons Attribution License (https://creativecommons.org/licenses/by/4.0/), which permits unrestricted reuse, distribution, and reproduction in any medium, provided the original work is properly cited.

Downloaded from academic.oup.com/mnras/article/550/1/stag1104/8705434 by Sarah Dakin user on 15 September 2026

2021). The spectrum also showed narrow emission components ($v \lesssim 300\,\mathrm{km\,s^{-1}}$), consistent with CSM interaction (O. D. Fox & N. Smith 2019; L. Dessart et al. 2021). The Cow showed polarization of $\sim$7 per cent at 5.7 d post-explosion, which quickly faded to show no polarization after 8 d except for a $\lesssim 1$ day increase to $\sim$ 1.5 per cent in the blue at 13 d (P. S. Smith et al. 2018; J. R. Maund et al. 2023). Follow-up observations also found a persistent UV source coincident with the Cow at $\sim$years post-explosion (N.-C. Sun et al. 2022, 2023; A. Inkenhaag et al. 2023, 2025; Y. Chen et al. 2023a, b).

The Cow was also bright at other wavelengths. Soft X-ray emission was detected shortly after the explosion (L. E. Rivera Sandoval et al. 2018 ; N. P. M. Kuin et al. 2019), and followed a shallow temporal decline until steepening at $\sim$ 20 d, when the optical lines at $\sim$3000–4000 km s^{-1} emerged (R. Margutti et al. 2019). The soft X-ray light curve was highly variable, and quasi-periodic oscillations (QPOs) were claimed at 225 Hz (D. R. Pasham et al. 2021) and 4 mHz (D. Xiang et al. 2021), giving constraints on the mass of the central object to be <850 $\mathrm{M_\odot}$ and 10^3–10^5 $\mathrm{M_\odot}$, respectively. The persistent source found at $\sim$ years post-explosion also showed soft X-ray emission (G. Migliori et al. 2024). The Cow also showed bright hard X-ray, radio, and millimetre emission (A. Y. Q. Ho et al. 2019; R. Margutti et al. 2019; A. J. Nayana & P. Chandra 2021). The radio evolved smoothly and showed a steep temporal drop at $\sim$ 1 month (A. Y. Q. Ho et al. 2019), indicating a different origin from the X-rays. The atypical properties of the radio compared to radio SNe can be understood if the radiating electrons have a relativistic Maxwellian energy distribution (B. Margalit & E. Quataert 2021; A. Y. Q. Ho et al. 2022; B. Margalit & E. Quataert 2024).

The multiwavelength analysis from R. Margutti et al. (2019) found that the observed properties of the Cow can be explained by a central engine surrounded by an aspherical ejecta with a trans-relativistic polar component and a lower velocity equatorial ring or torus. The central engine hypothesis for LFBOTs is also supported by the time variability of the X-rays, giant optical flares from AT2022tsd (A. Y. Q. Ho et al. 2023a), possible QPOs, and long-lasting UV/X-ray remnant. The radio emission is likely caused by the interaction between the trans-relativistic component and surrounding high density (10^5 cm^{-3}), wind-like CSM (A. Y. Q. Ho et al. 2019; R. Margutti et al. 2019) on scales of $\sim 10^{16}$ cm. For wind speeds of $\sim$1000 km s^{-1} (typical of Wolf–Rayet stars), the mass loss rate is implied to be $\dot{M} = 10^{-4}$–10^{-3} $\mathrm{M_\odot}$ yr^{-1} (R. Margutti et al. 2019), which is more than an order of magnitude higher than expected in Wolf–Rayet stars (M. J. Barlow, L. J. Smith & A. J. Willis 1981; T. Nugis & H. J. G. L. M. Lamers 2000; A. Adhyaqsa et al. 2020). This indicates either an extended CSM or a distinct physical origin (O. D. Fox & N. Smith 2019). In the early phase, the opticaal emission from the polar component is thought to arise from reprocessed X-ray emission from the central engine (A. L. Piro & W. Lu 2020; K. Uno & K. Maeda 2020a; D. Calderón, O. Pejcha & P. C. Duffell 2021; C. Chen & R.-F. Shen 2022; K. Uno & K. Maeda 2023). The photosphere from this component recedes into the equatorial torus as reprocessing becomes less efficient on the time-scale where the lower velocity lines emerge.

Since the discovery of the Cow, a few other transients have been discovered with similar properties. These include AT2018lug/ZTF18abvkwla ('the Koala', A. Y. Q. Ho et al. 2020), CSS161010 (D. L. Coppejans et al. 2020; C. P. Gutiérrez et al. 2024), AT2020xnd/ZTF20acigmel ('the Camel', D. A. Perley et al. 2021; J. S. Bright et al. 2022; A. Y. Q. Ho et al. 2022), AT2020mrf (Y. Yao et al. 2022), AT2022tsd ('the Tasmanian Devil', D. Matthews et al. 2023; A. Y. Q. Ho et al. 2023a), and AT2023fhn ('the Finch', A. A. Chrimes et al. 2024a, b). These objects show some variety in peak luminosity and ejecta velocity, but all show hot, roughly featureless early spectra, optical luminosities similar to SLSNe, and bright X-ray and radio emission. J. J. Somalwar et al. (2025) also discovered AT2024puz, which has similar properties to both LFBOTs and TDEs and evolves on a time-scale intermediate between the two. The LFBOT rate is estimated to be <0.1 per cent of the core-collapse SN rate (A. Y. Q. Ho et al. 2023b), and they normally occur in metal-poor, low-mass starburst galaxies (A. Y. Q. Ho et al. 2019; M. J. Michałowski et al. 2019; D. L. Coppejans et al. 2020; J. D. Lyman et al. 2020; Y. Yao et al. 2022). These environments are similar to those of Type-I SLSN and long gamma-ray burst (GRB) progenitors (R. Lunnan et al. 2014; T. W. Chen et al. 2015; G. Leloudas et al. 2015; C. R. Angus et al. 2016; T.-W. Chen et al. 2017; S. Schulze et al. 2018; S. V. Ørum et al. 2020), which may indicate that these transients all come from massive, low-metallicity progenitors.

Although the ejecta structure of LFBOTs is somewhat understood, the nature of the progenitor that produces it is still unknown. A few proposed scenarios include engine-driven SNe (e.g. S. J. Prentice et al. 2018; J.-F. Liu et al. 2022; C. M. B. Omand & N. Sarin 2024), failed SNe with prompt accretion disc formation (R. Margutti et al. 2019; D. A. Perley et al. 2019; E. Quataert, D. Lecoanet & E. R. Coughlin 2019), tidal disruption events (TDEs) from intermediate mass black holes (IMBHs; N. P. M. Kuin et al. 2019; D. A. Perley et al. 2019; C. P. Gutiérrez et al. 2024), choked jets (O. Gottlieb, A. Tchekhovskoy & R. Margutti 2022; N. Soker 2022; A. Suzuki & K. Maeda 2022; A. Suzuki, C. M. Irwin & K. Maeda 2024; H. Hamidani et al. 2025b), highly aspherical SNe ('ellipsars', M. DuPont, A. MacFadyen & J. Zrake 2022), and the merger of a compact object and massive star (M. Lyutikov & S. Toonen 2019; S. L. Schrøder et al. 2020; K. Uno & K. Maeda 2020a; B. D. Metzger 2022a). CSM-interaction models have also been proposed (O. D. Fox & N. Smith 2019; D. Xiang et al. 2021; C. Pellegrino et al. 2022; D. K. Khatami & D. N. Kasen 2024), but these are disfavoured due to the variability and long duration of the X-ray emission. The central X-ray source could be either a magnetized nebula (e.g. C. M. B. Omand, K. Kashiyama & K. Murase 2018; I. Vurm & B. D. Metzger 2021; C. M. B. Omand, N. Sarin & G. P. Lamb 2025b), which can cause ejecta asymmetry due to Rayleigh-Taylor instabilities between the wind and ejecta (J. M. Blondin & R. A. Chevalier 2017; A. Suzuki & K. Maeda 2017, 2021; C. M. B. Omand, N. Sarin & T. Temim 2025a); the inner region of a Super-Eddington accretion disc (A. Sądowski & R. Narayan 2015); or a choked jet (O. Gottlieb et al. 2022). The transients can be infrared bright due to the dense outflow creating a light echo (B. D. Metzger & D. A. Perley 2023; J.-Y. Li et al. 2025) or from newly formed dust reprocessing emission from the central engine (C. M. B. Omand, K. Kashiyama & K. Murase 2019).

One of the newest additions to the LFBOT class is AT2024wpp ('the Whippet' A. Y. Q. Ho et al. 2024). AT2024wpp is one of the closest ($z = 0.0868$; D. A. Perley et al. 2024) and brightest ($L_{\mathrm{bol,peak}} > 10^{45}$ erg s^{-1}) LFBOTs to date, and the first one to be identified before the optical/UV peak (A. Y. Q. Ho et al. 2024). A comprehensive multiwavelength dataset on the object has been collected, including NIR/optical/UV photometry and spectroscopy, optical polarization, radio and millimetre data, and X-ray data (R. Margutti et al. 2024; G. Schroeder, A. Y. Q. Ho & D. A. Perley 2024; G. Srinivasaragavan et al. 2024; A. J. Nayana

Downloaded from academic.oup.com/mnras/article/550/1/stag1104/8705434 by Sarah Dakin user on 15 September 2026

et al. 2025; M. Pursiainen et al. 2025; N. LeBaron et al. 2026; D. A. Perley et al. 2026). AT2024wpp is featureless at early epochs, but shows weak H and He features after ~ 30 d. Late-time observations show no evidence for minute-time-scale flares (E. O. Ofek et al. 2025) similar to AT2022tsd (A. Y. Q. Ho et al. 2023a). The optical peak is well described by a $\gtrsim$30 000 K blackbody, and the optical component remains well-described by a $\gtrsim$20 000 K blackbody out to late times, although there is some evidence for a power-law NIR excess after ~ 20 d. The X-ray emission hardens over time and shows a rebrightening at $\sim$50 d. The radio emission rises quickly over $\sim$20–30 d before starting to decline.

This work attempts to find a physically plausible scenario for AT2024wpp that can explain both the thermal and non-thermal emission. We approach this task by fitting several semi-analytic models to each component and using the results of those fits to determine whether different scenarios are viable. We summarize the data we attempt to model in Section 2 and the models used in Section 3. The results are shown in Section 4 and discussed in Section 5. Finally, we conclude in Section 6.

2 DATA MODELLED

The data we model include the NIR/optical/UV photometry, radio data, and X-ray data presented in D. A. Perley et al. (2026). The photometry was gathered using a number of surveys and facilities, including the Zwicky Transient Facility (ZTF; M. J. Graham et al. 2019; E. C. Bellm et al. 2019b; R. Dekany et al. 2020) using the Samuel Oschin 48-inch Schmidt telescope, IO:O and the Liverpool Infra-Red Imaging Camera (LIRIC) on the Liverpool Telescope, the Rainbow Palomar 60-inch telescope at Palomar Observatory, the Panoramic Survey Telescope and Rapid Response System (Pan-STARRS), Goodman High-Throughput Spectrograph (GHTS) on the Southern Astrophysical Research Telescope (SOAR), the ESO Faint Object Spectrograph and Camera v2 (EFOSC2) on the New Technology Telescope (NTT), the Focal Reducer/Low Dispersion Spectrograph 2 (FORS2) on the Very Large Telescope (VLT), the Ultraviolet-Optical Telescope (UVOT) on the Neil Gehrels *Swift* Observatory, and the Wide Field Camera 3 (WFC3) on the *Hubble Space Telescope* (*HST*). X-ray observations were taken by the *X-Ray Telescope* (*XRT*) on *Swift*, and the radio observations were taken by the Karl G. Jansky Very Large Array (VLA) and Atacama Large Millimetre/submillimetre Array (ALMA). Overall, the UVOIR photometric data has detections spanning $\sim$120 d and upper limits at $\sim$150–220 d after the last detection. The radio data spans the 3.0–350 GHz frequency range and has detections up to $\sim$200 d post-discovery. The X-ray data are only in one band (0.2–10 keV), and lasts $\sim$80 d. Upper limits were not included in model fits in either the optical or non-thermal models, although late-time upper limits are used as constraints in Section 5.

3 MODELS AND FITTING

We test various models by performing Bayesian inference to fit them to the multiband optical photometry and radio data using REDBACK[1] (N. Sarin et al. 2024). We use the PYMULTINEST sampler (J. Buchner et al. 2014) implemented in BILBY (G. Ashton et al. 2019), and sample in flux density with a Gaussian likelihood. The priors used are listed in Appendix A. We sample the initial time with a uniform prior of up to 20 days before the first observation, and include a host extinction term A_V with a uniform prior between 0 and 2 mag for the optical data. A list of the models used is given in Table 1.

The first model used is an evolving blackbody model, which fits the transient by assuming the photospheric temperature and radius both have power-law rises and declines in time. The temperature and radius peaks are not assumed to be at the same time. While this will not reveal the physics of the LFBOT, it will allow us to characterize the photospheric radius and temperature of the system, which can provide insight into the properties that the more physical models need to have in order to describe the data.

The physical semi-analytic optical models we test can be divided into a few broad classes: SNe, shock cooling, TDEs, and stellar mergers. These models were chosen to represent the wide range of phenomena that could potentially explain LFBOTs. These models all calculate the bolometric luminosity and photospheric radius of one or more components, and convert that to observed emission by assuming each component is described by a blackbody spectral energy distribution.

3.1 Supernova models

We test four SN models, which differ depending on their power source. One is the standard ^{56}Ni-powered SN, known as the Arnett model (S. A. Colgate & C. McKee 1969; W. D. Arnett 1982). This model usually has difficulty explaining transients with high luminosities and low diffusion times, due to the constraint that the ^{56}Ni mass must be lower than the ejecta mass. The other SNe models also have ^{56}Ni, but are primarily powered by a different source. One model is the millisecond magnetar model (C. M. B. Omand & N. Sarin 2024), which was shown in C. M. B. Omand & N. Sarin (2024) to be a good fit to the LFBOT AT2020xnd ('the Camel', D. A. Perley et al. 2021). Another is the CSM interaction model (E. Chatzopoulos et al. 2013; V. A. Villar et al. 2017; B. Jiang et al. 2020), powered by the conversion of kinetic energy into luminosity via the shock formed between the ejecta and CSM. The final one is the fallback SN model (J. Guillochon et al. 2018), which is powered by the accretion of material onto a central black hole remnant.

3.2 Shock cooling models

Shock cooling emission is the radiation from shock heated material as it cools and expands after shock breakout (e.g. B. Margalit 2022). The shock that heats the material can come from either an SN explosion or a GRB jet, leaving a region of shocked material called the cocoon. The material can either be the envelope of the star or an extended CSM. This leads us to examine four shock cooling scenarios: the SN + envelope (N. Sapir & E. Waxman 2017), SN + extended CSM (A. L. Piro et al. 2021), cocoon + envelope (A. L. Piro & W. Lu 2020), and cocoon + extended CSM (H. Hamidani et al. 2025a, b). Shock cooling can emit on short time-scales but cannot produce emission at later times, so we test all the shock cooling models alongside a ^{56}Ni component to better explain late-time emission.

3.3 Tidal disruption event models

We test three models for TDE emission, which vary how the optical emission is produced after the star is disrupted. None of the models self-consistently solve the early pre-circularization

[1]Version 1.15.1

Downloaded from academic.oup.com/mnras/article/550/1/stag1104/8705434 by Sarah Dakin user on 15 September 2026

Table 1. The optical, radio, and X-ray models used to fit the data for AT2024wpp, and their associated references.

Model	REDBACK Model Name	Reference
	Optical	
Evolving blackbody	evolving_blackbody	N. Sarin et al. (2024)
^{56}Ni-powered SN	arnett	W. D. Arnett (1982)
Magnetar-powered SN	general_magnetar_driven_supernova	N. Sarin et al. (2022) and C. M. B. Omand & N. Sarin (2024)
CSM-powered SN	csm_nickel	E. Chatzopoulos et al. (2013), V. A. Villar et al. (2017), and B. Jiang, S. Jiang & V. Ashley Villar (2020)
Fallback-powered SN	sn_nickel_fallback	J. Guillochon et al. (2018)
SN + envelope shock cooling	shockcooling_sapirwaxman_and_arnett	N. Sapir & E. Waxman (2017)
SN + CSM shock cooling	shock_cooling_and_arnett	A. L. Piro, A. Haynie & Y. Yao (2021)
Cocoon + envelope shock cooling	shocked_cocoon_and_arnett	A. L. Piro & J. A. Kollmeier (2018)
Cocoon + CSM shock cooling	shocked_cocoon_csm_and_arnett	H. Hamidani et al. (2025a, b)
Fallback TDE	tde_fallback	J. Guillochon & E. Ramirez-Ruiz (2013), J. Guillochon et al. (2018), and B. Mockler, J. Guillochon & E. Ramirez-Ruiz (2019)
Stream–stream collision TDE	stream_stream_tde	T. Piran et al. (2015) and T. Ryu, J. Krolik & T. Piran (2020)
Cooling envelope TDE	gaussianrise_cooling_envelope	B. D. Metzger (2022b) and N. Sarin & B. D. Metzger (2024)
BH–WR merger	wr-bh_merger	B. D. Metzger (2022a)
	Radio and X-ray	
Top-hat Jet	tophat_redback	G. P. Lamb, I. Mandel & L. Resmi (2018)
Gaussian Jet	gaussian_redback	G. P. Lamb et al. (2018)
Power-law synchrotron	synchrotron_pldensity	S. Rosswog & M. Brüggen (2007) and R. A. Chevalier & C. Fransson (2017)
Thermal synchrotron	thermal_synchrotron_v2_fluxdensity	B. Margalit & E. Quataert (2021, 2024)
Accretion disc	fitted	A. Mummery & S. A. Balbus (2020) and A. Mummery et al. (2024, 2025)
Top-hat Jet + accretion Disc	tophat_redback & fitted	

emission, and instead they all assume a constant-temperature Gaussian rise until peak. The first model assumes the emission is directly powered by fallback accretion onto the central black hole (J. Guillochon & E. Ramirez-Ruiz 2013; J. Guillochon et al. 2018; B. Mockler et al. 2019). The second model assumes the emission is powered by shocks resulting from the collisions of debris streams (T. Piran et al. 2015; T. Ryu et al. 2020). The final TDE model assumes the bound debris forms a quasi-steady envelope which cools radiatively as it undergoes Kelvin-Helmholtz contraction (B. D. Metzger 2022b; N. Sarin & B. D. Metzger 2024). For these models, we alter the default prior such that the lower bound of the black hole mass goes down to 1 $M_{\odot}$, since the TDE rise time is predominately set by the black hole mass and a time-scale of $\sim$ 5 d requires an intermediate or stellar mass black hole.

3.4 Stellar merger model

The final optical model is the disruption and hyper-accretion of a Wolf–Rayet star onto a black hole companion, with a delay between the common envelope phase and the merger (B. D. Metzger 2022a). The optical emission in this model is primarily powered by reprocessed X-rays from the inner accretion disc, although interaction between ejecta and CSM can also contribute at later times.

3.5 Radio and X-ray models

To try and explain the radio and X-ray emission, we test models from GRB afterglows, CSM interaction from non-relativistic or trans-relativistic spherical blast waves, and from an accretion disc. Since previous LFBOTs have shown evidence for multiple components in their non-thermal emission, the radio and X-ray data are fit separately. We test two jet structures for the afterglow: a top-hat jet and a Gaussian jet (G. P. Lamb et al. 2018). For CSM interaction, we test a power-law synchrotron model (S. Rosswog & M. Brüggen 2007; R. A. Chevalier & C. Fransson 2017), where the emitting electrons have a power-law energy distribution, and a thermal synchrotron model (B. Margalit & E. Quataert 2021, 2024), where the emitting electrons have a relativistic Maxwellian distribution. The GRB afterglow models are assumed to be in a constant density medium since they decelerate further away from the progenitor, while the interaction models are assumed to be in a medium with a power-law density profile $\rho \propto r^{-\alpha}$, with α between 0 and 4. The emission from the accretion disc is fit using models from FITTED (A. Mummery et al. 2025) imported into REDBACK, and we also examine a case with a jet and accretion disc.

4 RESULTS

4.1 Optical

Fig. 1 shows the multiband fit from the evolving blackbody model and the luminosity, photospheric radius, and temperature derived from it; the values found by D. A. Perley et al. (2026) are also shown as a comparison. The model provides a good fit to the overall, showing that a blackbody with power-law time dependence can approximate the system well. The inferred luminosities, radii, and temperatures also broadly agree with other measurements from N. LeBaron et al. (2026). The radius increase with power-law index $\sigma_{\rm R,rise} = 0.01^{+0.01}_{-0.01}$ and decreases with $\sigma_{\rm R,decline} = -1.06^{+0.01}_{-0.01}$, while the temperature rises with $\sigma_{\rm T,rise} = 1.02^{+0.01}_{-0.01}$ and declines with $\sigma_{\rm T,decline} = -0.35^{+0.01}_{-0.01}$, where R or $T \propto t^{\sigma}$. The luminosity indices are determined from R or T, which give an initial rise index of $4.10^{+0.06}_{-0.06}$, an intermediate decline index of $-1.38^{+0.06}_{-0.06}$, then a final decline index of $-3.52^{+0.06}_{-0.06}$. The inferred luminosities, radii, and temperatures do differ from D. A. Perley et al. (2026) at early times, likely due to the simplified power-law time evolution of those properties in our model, so inferred

Downloaded from academic.oup.com/mnras/article/550/1/stag1104/8705434 by Sarah Dakin user on 15 September 2026

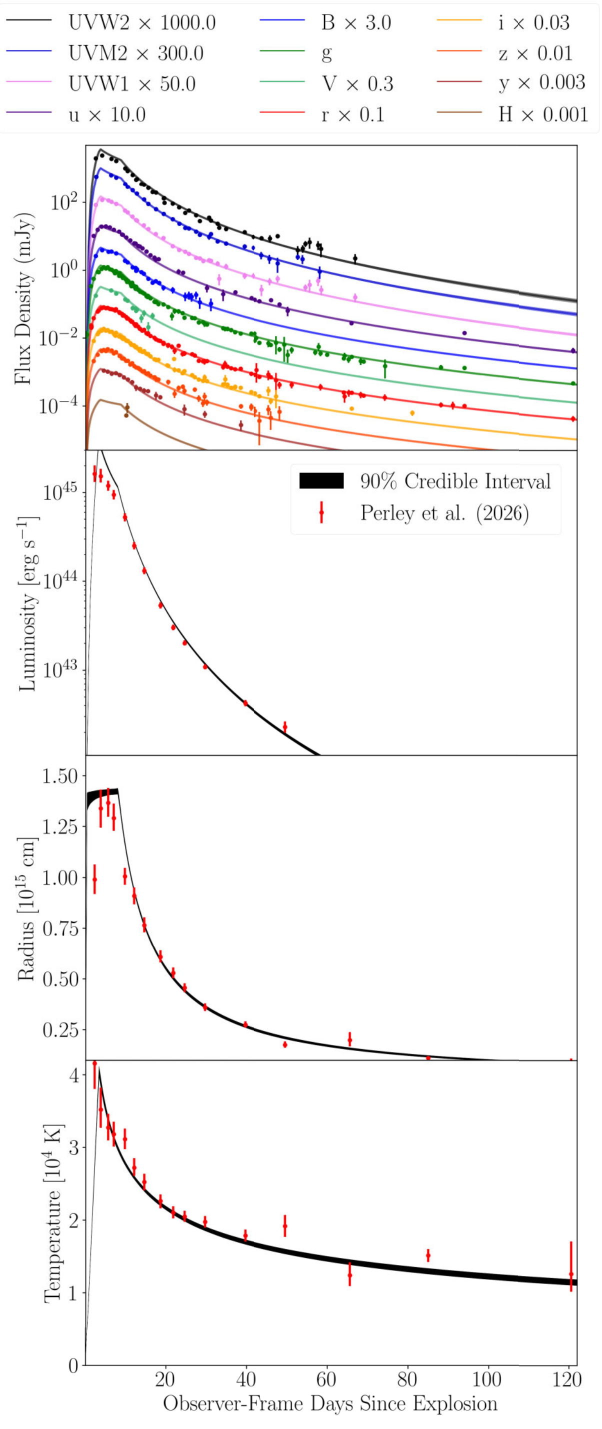

Figure 1. The multiband fit from the evolving blackbody (top) and the luminosity (second), radius (third), and temperature (bottom) derived from it. The shaded region shows the 90 per cent credible interval. The bottom three plots show values from D. A. Perley et al. (2026) for comparison.

parameters during the early and intermediate phases are likely unreliable.

Fig. 2 shows the fits to the optical data with the more physically-motivated models, with the posteriors listed in Appendix A. Several models, including the magnetar-powered SN model, SN + envelope shock cooling model, and black hole–Wolf Rayet (BH–WR) merger model, can reproduce the rise and decline time-scales, luminosity, and colour evolution of the light curve well. A few other models, including the nickel-powered and fallback-powered SN models as well as the cocoon + envelope and SN + CSM shock cooling models, can somewhat reproduce the data but underpredict the UV emission around peak. The TDE models all fail to describe the data, with the fallback and stream-stream collision models evolving much too slowly, and the cooling envelope model cooling far too quickly.

The parameters for each of the SN, shock cooling, and BH–WR merger models all contain a plateau temperature, $T_{\rm floor}$, which has a wide prior between 10^3 and 10^5 K. Models with this parameter keep the photospheric temperature at a minimum value $T_{\rm floor}$ at late times, resulting in the photospheric radius receding as the luminosity continues to decrease. This allows the models to approximate a time when the photosphere recedes without the need to continuously calculate the optical depth of the ejecta. M. Nicholl, J. Guillochon & E. Berger (2017) mention that this parameter may contain information about other processes keeping the ejecta at a constant temperature, such as recombination or ejecta fragmentation from a central engine. Using $T_{\rm floor}$ also allows the model to make multiband predictions deep into the nebular phase, when the photosphere no longer exists and the emission can no longer have a blackbody spectrum. Emission at this phase is driven mostly by line emission in supernovae, although in LFBOTs, free–free emission and non-thermal emission from the heating source may also be important. Because of this, a blackbody approximation can not make accurate predictions past the photospheric phase (see discussion in S. Schulze et al. 2024).

The values of $T_{\rm floor}$ from the fits shown in Fig. 2 are between 20 000–40 000 K, similar to the values found for the LFBOT AT2020xnd by C. M. B. Omand & N. Sarin (2024). This is much higher than the ∼5000 K that has been estimated for other transients (M. Nicholl et al. 2017; F. Taddia et al. 2019). This implies the photosphere begins to recede early, which is consistent with the data. However, this also implies that the ejecta becomes optically thin within $\lesssim 10$ d (see Appendix B), which is not consistent with the spectroscopic data (D. A. Perley et al. 2026).

We re-fit the optical data with the same models, but with the upper limit on the prior for $T_{\rm floor}$ set to 10^4 K – these fits are shown in Fig. 3 with the posteriors listed in Appendix A. $T_{\rm floor} \leq 10^4$ K was chosen because it is below the inferred late-time temperature of the LFBOT (Fig. 1), so a model would have to self-consistently calculate the photospheric radius and temperature to explain the data. The TDE models do not use $T_{\rm floor}$, and thus remain unchanged. Most models now cool to $\leq 10^4$ K on time-scales comparable to the peak of the LFBOT or earlier, and fail to reproduce the UV data. Only the magnetar-driven SN model and BH–WR merger model can reproduce the light curve peak, but cool down shortly after and fail to reproduce the observed decline, again underpredicting the UV data.

4.2 Radio and X-ray

Fig. 4 shows the fits to the radio and X-ray data, which were modelled separately to allow for the possibility that they could arise from separate processes. The posteriors are listed in Appendix A. The radio data are better reproduced by the two afterglow models and the power-law synchrotron blast wave model compared to the thermal synchrotron blast wave model. Specifically, the afterglows and power-law synchrotron show a more pronounced peak on the same time-scale as the data and a

Downloaded from academic.oup.com/mnras/article/550/1/stag1104/8705434 by Sarah Dakin user on 15 September 2026

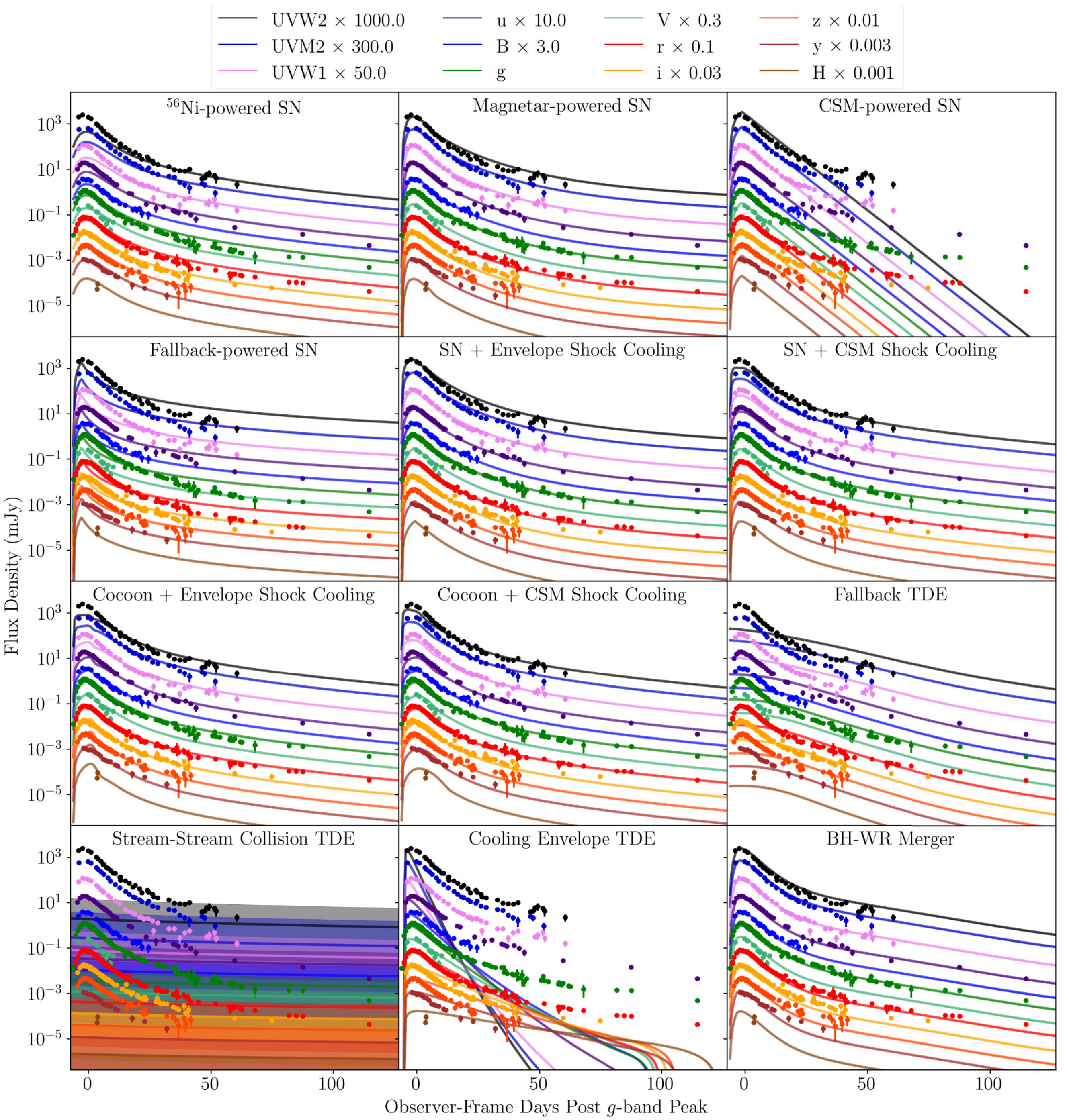

Figure 2. The light curve fits to the broadband optical data for each model discussed in Section 3 (see Table 1) using default priors. The solid line shows the model with the highest likelihood while the shaded region shows the 90 per cent confidence interval.

faster decline, although none of the models can reproduce the fast decline consistent with the 3 GHz upper limit. The jets are both predicted to be strongly off-axis, with $\theta_{\rm obs}/\theta_{\rm core} \sim 5$–10. The power-law synchrotron is predicted to be in a medium with $\rho \overset{\propto}{\sim} r^{-2.9}$. The fits to the X-ray data show a different preference; the synchrotron blast wave models reproduce the later data well but underpredict the early data, while the jet and accretion disc models fail to reproduce the data entirely, especially at late times.

An important consideration from the radio and X-ray fits is what they predict for the opposite band, since a model that overpredicts the other band would not be a viable candidate. Fig. 5 shows the fits presented in Fig. 4 extended into the opposite band. The two jet models and power-law synchrotron model from the X-ray data all have wide confidence intervals that roughly overlap with the radio data, while the thermal synchtrotron model overpredicts the radio data and the accretion disc and jet + accretion disc models underpredict. The models that are consistent with

Downloaded from academic.oup.com/mnras/article/550/1/stag1104/8705434 by Sarah Dakin user on 15 September 2026

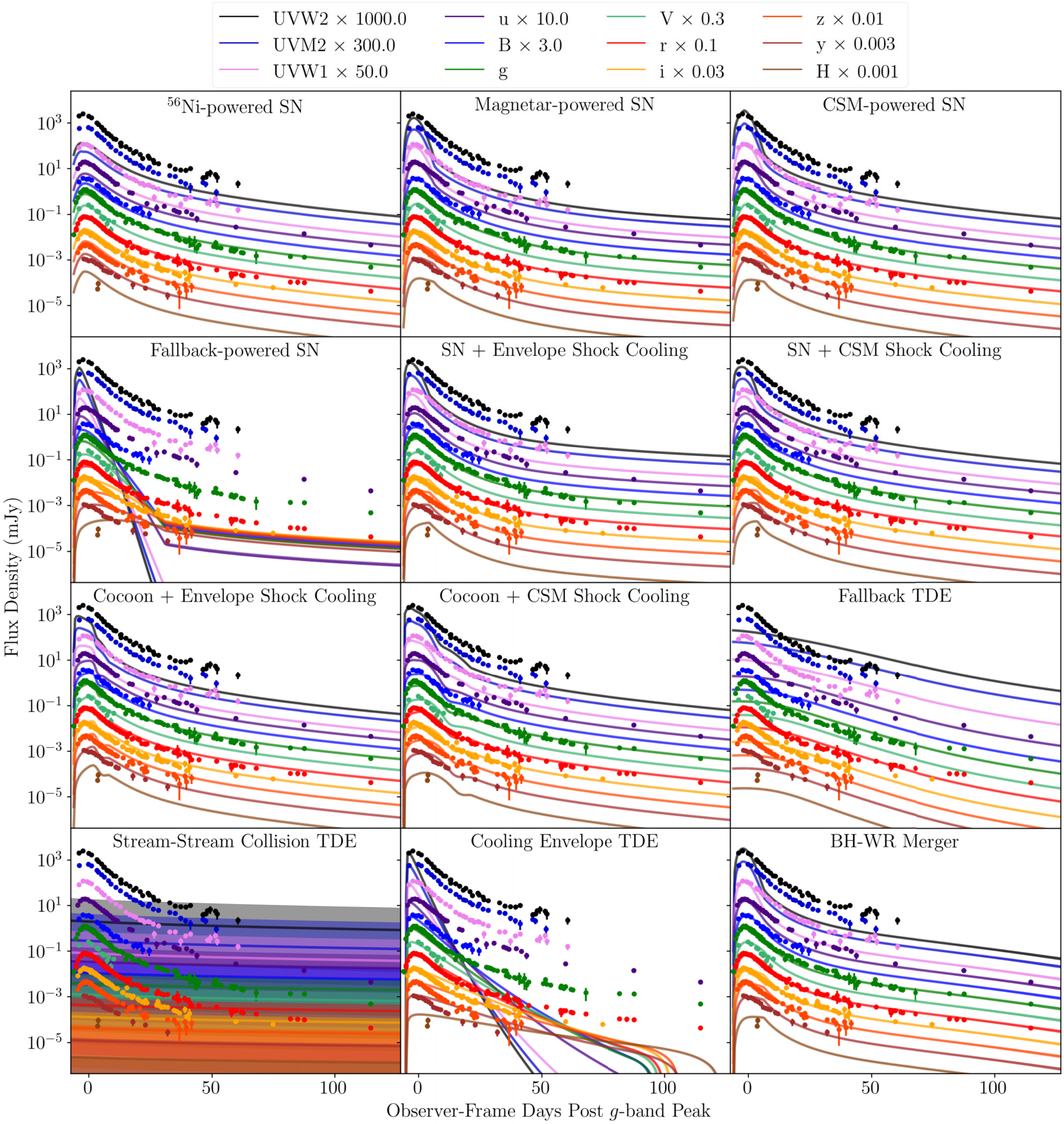

Figure 3. Same as Fig. 2, but with the prior for $T_{\rm floor}$ restricted to $< 10^4$ K.

the radio data show very different behaviours in the X-ray, with the Gaussian jet severely underpredicting the data; thermal synchrotron being consistent with the late data but underpredicting the early data; the top-hat jet being roughly consistent but showing a rise on the time-scale of 25 d, which is not observed; and the power-law synchrotron model overpredicting the data by an order of magnitude.

Putting these results together yields no obvious explanation for the non-thermal emission. The radio could be explained by an off-axis Gaussian jet, since the X-ray flux of that model does not overpredict the data. The X-ray flux is only consistent with the synchrotron models, but the thermal synchrotron overpredicts the radio data. The power-law synchrotron models from the X-ray fits are roughly consistent with the radio data, yet the models from the radio fits overpredict the X-ray data by more than an order of magnitude. If the X-rays are powered by a power-law synchrotron blast wave, there may be emission from a second component, like an off-axis jet, that can better reproduce the early

Downloaded from academic.oup.com/mnras/article/550/1/stag1104/8705434 by Sarah Dakin user on 15 September 2026

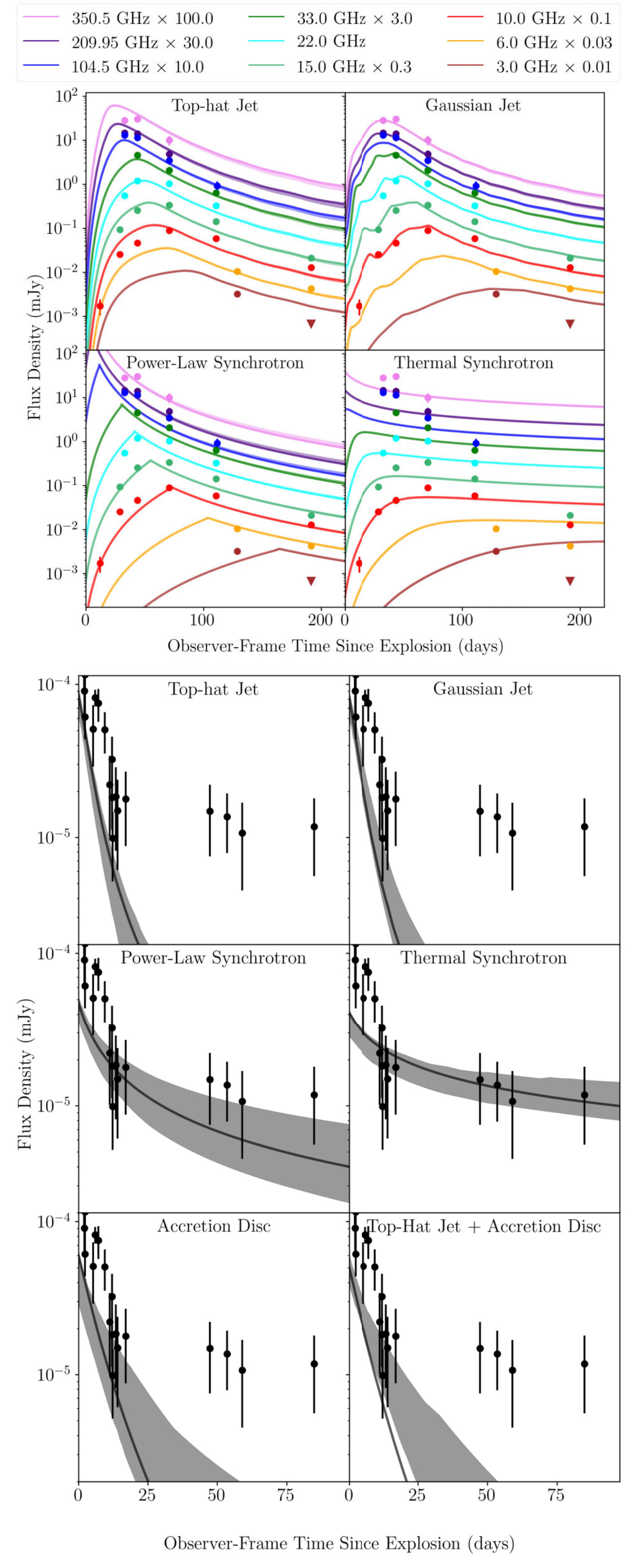

Figure 4. The light curve fits to the radio and submillimetre (top) and X-ray (bottom) data for each model discussed in Section 3 (see Table 1). The solid line shows the model with the highest likelihood while the shaded region shows the 90 per cent confidence interval.

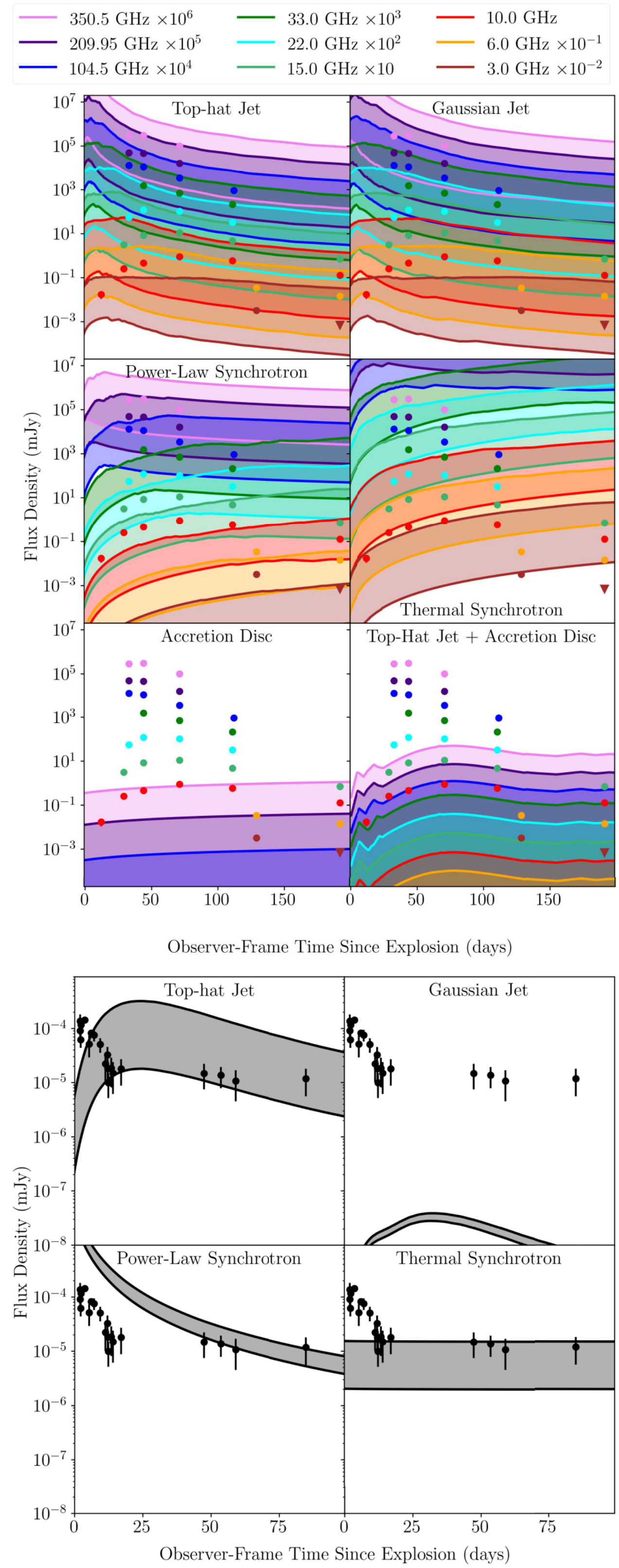

Figure 5. Radio light curves using the posteriors from the X-ray fits (top) and X-ray light curves using the radio posteriors (bottom) (see Fig. 4 for the fits). The shaded region shows the 90 per cent confidence intervals, while the solid lines show the upper and lower bounds of the 90 per cent confidence intervals.

Downloaded from academic.oup.com/mnras/article/550/1/stag1104/8705434 by Sarah Dakin user on 15 September 2026

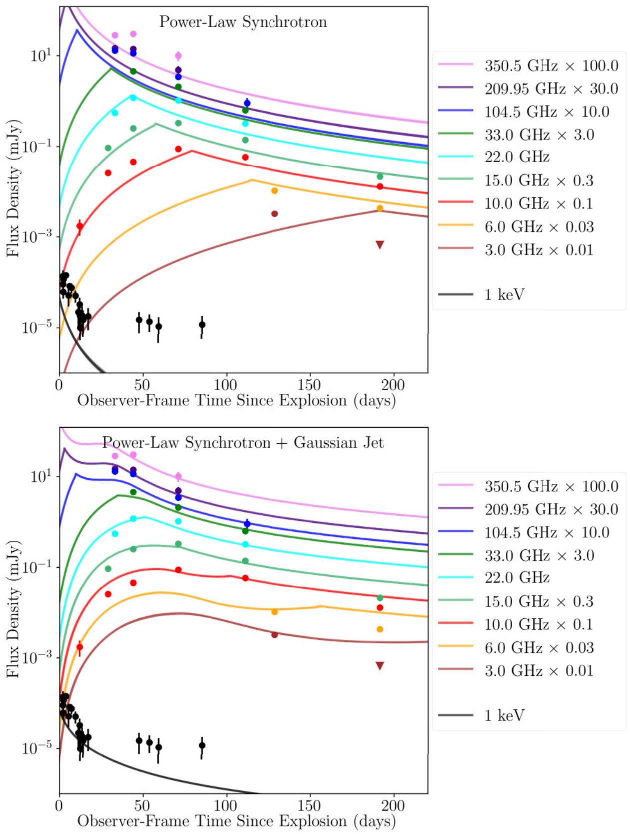

Figure 6. The light-curve fits to the radio, submillimetre, and X-ray data for the power-law synchrotron (top) and thermal synchrotron (bottom) models. The solid line shows the model with the highest likelihood while the shaded region shows the 90 per cent confidence interval.

radio emission, but that component would need to have a radio flux not significantly larger than the blast wave and a negligible X-ray flux.

The two possibilities to explain the non-thermal emission that arise from our analysis, assuming that the data are not described by a model we have not investigated, are that a power-law synchrotron blast wave can explain both the radio and X-ray data, or that a combined Gaussian jet and power-law synchrotron blast wave are needed to explain the data. We show the combined radio and X-ray fits for both of these scenarios in Fig. 6, with the posteriors listed in Appendix A. The power-law synchrotron fit is similar to the fits presented in Fig. 4: The model underpredicts X-rays at early times but reproduces the data at late times, and does not reproduce the peak or the decline in the radio data. The synchrotron + Gaussian jet model reproduces the peak and decline in the radio data, but underpredicts the X-ray data. While neither of these possibilities can explain the data, this might be due to these models assuming a power-law density profile for the CSM. A more complicated profile may be able to explain the differences at late time for the radio (see discussion in Section 5.3), although it seems likely that the X-ray emission was produced by a process we have not considered here.

5 DISCUSSION

5.1 Model analysis and late-time predictions

The optical models tested all failed to reproduce the optical emission unless the temperature was allowed to plateau at $>20\,000$ K. This highlights the need for multiband fitting when examining light-curve models, as opposed to bolometric fitting. After the diffusion phase, a constant temperature implies $L \propto R_{\rm phot}^2$, which may be a good approximation when the photosphere is receding. The recession of the photosphere in an expanding medium begins when the optical depth of the ejecta drops fast enough to counteract the effect of the ejecta expansion. This time-scale can be connected to the nebular time-scale, when the entire ejecta becomes optically thin. Appendix B shows that the ratio between these two time-scales for a homologously expanding medium with any non-increasing density profile is $< \sqrt{3}$. While the data show the photospheric radius peaks on a time-scale of $\sim$5 d, spectra at $\sim$ 40 d still show the emission being dominated by a blackbody-like continuum (D. A. Perley et al. 2026). Since this is inconsistent with the derived time-scales, this suggests that the ejecta responsible for the thermal emission cannot be homologously expanding, which rules out the SN, shock cooling, and BH–WR merger models. This can also rule out some models we did not test, such as the TDE-powered SN model from D. Tsuna & W. Lu (2025) or the Helium core-black hole merger from J. Klencki & B. D. Metzger (2025). This does not rule out the presence of homologous components that may produce spectral lines or non-thermal emission, but these components cannot be the primary source of the optical emission. This photospheric behaviour also does not rule out TDEs, although none of the TDE models were able to explain the optical emission. However, TDE models are known to be uncertain and the emission processes of supermassive black hole (SMBH) TDEs, especially around peak are not well understood (e.g. N. Sarin & B. D. Metzger 2024; C. R. Angus et al. 2026; J. L. Wise et al. 2026), so the possibility that this transient could be an IMBH TDE cannot be completely discounted. The lack of early rest-frame optical/near-UV spectral features may point to AT2024wpp as a low-mass analogue to featureless TDEs (E. Hammerstein et al. 2023). However, the presence of the dense extended material inferred from radio emission is not predicted by any current TDE models.

One way of testing models is using their early properties to predict emission at later times (e.g. C. J. Law et al. 2019; R. Margutti et al. 2023; C. M. B. Omand & A. Jerkstrand 2023). The late-time emission from tidal disruption events can be predicted in radio (e.g. B. A. Zauderer et al. 2011; S. Velzen et al. 2016; I. Andreoni et al. 2022; K. D. Alexander et al. 2026), infrared (e.g. L. Dou et al. 2016; M. Masterson et al. 2024; M. Newsome et al. 2024), X-rays (e.g. N. Bade, S. Komossa & M. Dahlem 1996; J. L. Donley et al. 2002; I. Grotova et al. 2025), and may also be in neutrinos (e.g. R. Stein et al. 2021; N. Jiang et al. 2023; S. Ji et al. 2025; S. Toshikage et al. 2025). One prediction from all TDE models is that the system will settle into an accretion disc at late times, which will emit primarily in optical/UV and X-rays (A. Mummery et al. 2025). Since the TDE models for early optical emission did not reproduce the data for AT2024wpp, we do not use the posteriors from those models for predictions. We instead present F225W UV and 1 keV predictions[2] for 10^3 and 10^5 $M_\odot$ black holes and 0.5 and 5.0 $M_\odot$

[2] These predictions were made using the GR_DISC model from FITTED (A. Mummery et al. 2025), which ignores relativistic photon deflection and

Downloaded from academic.oup.com/mnras/article/550/1/stag1104/8705434 by Sarah Dakin user on 15 September 2026

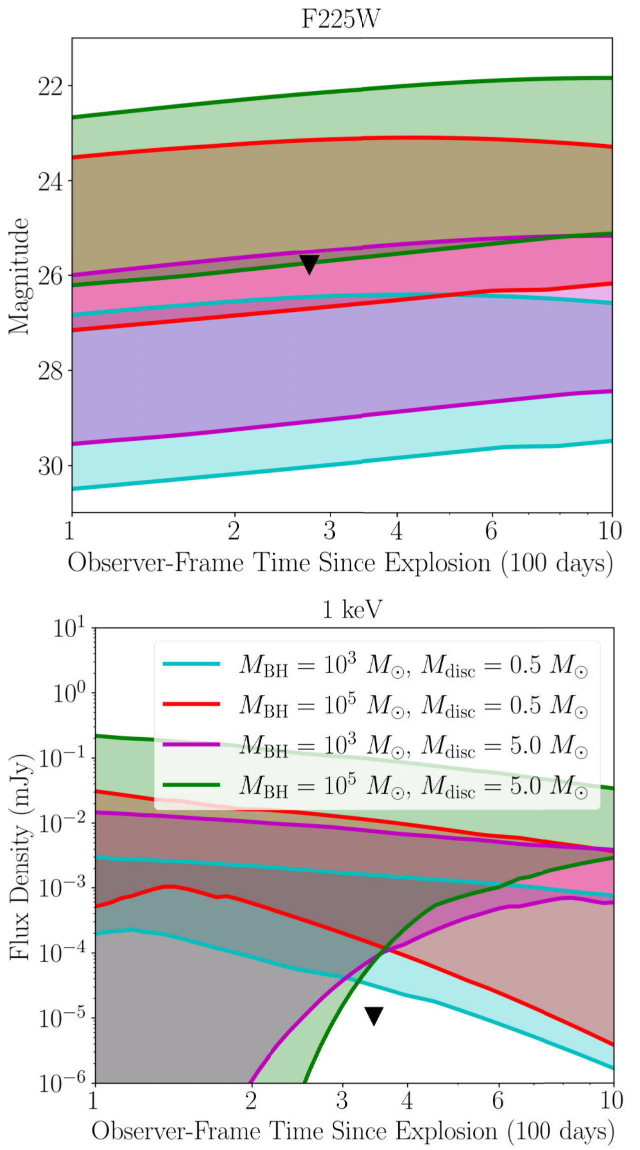

Figure 7. The predicted late-time emission from the accretion disc of an IMBH TDE. Each colour represents a different black hole mass and disc mass, while the width of the band shows the 90 per cent confidence interval from marginalizing over the default priors for the other parameters (see A. Mummery et al. (2025) for details). The solid lines show the upper and lower bounds of the 90 per cent confidence interval. The top panel shows the prediction for F225W, while the bottom panel shows the predictions at 1 keV. The triangles denote the observed 3σ upper limits.

accretion discs in Fig. 7. These black hole masses were chosen because the plateau emission from AT2018cow was estimated to originate from a $\sim 10^3\,M_\odot$ black hole (A. Inkenhaag et al. 2023, 2025), with $10^5\,M_\odot$ acting as a conservative upper limit. The observer-inclination angle and black hole spin are marginalized over using their default priors (A. Mummery et al. 2025), while the initial disc radius r_0 and viscous time-scale t_{visc} are calculated

gravitational redshift. Marginalizing over a prior using a model incorporating these effects (GR_DISC_PLUS) would be computationally unfeasible. These effects are not expected to strongly affect optical/UV emission, but may introduce uncertainty in the X-ray predictions.

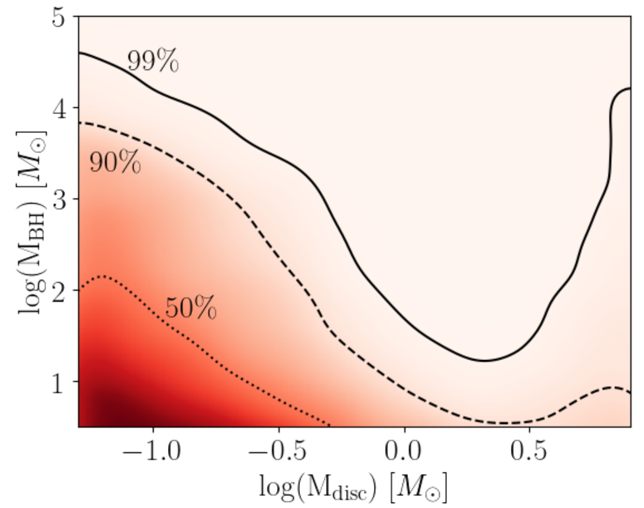

Figure 8. The viable region for plateau emission given the late-time UV and X-ray upper limits in an IMBH TDE. The darker regions indicate a high posterior density. The dotted, dashed, and solid lines indicate parameter regions excluded at 50 per cent, 90 per cent, and 99 per cent confidence, respectively.

via

$$r_0 = 2R_\star (M_{BH}/2M_{disc})^{1/3} \tag{1}$$

and

$$t_{visc} = \mathcal{V}\sqrt{r_0^3/GM_{BH}}. \tag{2}$$

We use the mass–radius relation $R_\star = (M_\star/M_\odot)^{4/5} R_\odot$ appropriate for lower-mass main sequence stars (B. D. Metzger 2022b; N. Sarin & B. D. Metzger 2024), and the parameter $\mathcal{V}$ encapsulates the poorly understood MHD effects in the disc physics. We sample $\mathcal{V}$ with a log-uniform prior between 10^2 and 10^4. Shown also are 3σ upper limits from D. A. Perley et al. (2026).

The F225W predictions have $\sim$3 mag of uncertainty, with the $10^5\,M_\odot$ black holes having emission between 22–26th mag and the $10^3\,M_\odot$ black holes having emission between 26–30th mag, making it likely this emission could be detected if the black hole mass is close to the IMBH–SMBH boundary, but more parameter dependent if the black hole mass is lower. The X-ray predictions have $\gtrsim$ an order of magnitude of uncertainty, especially during the first year, but are predicted to be between $\sim 10^{-1} - 10^{-5}$ mJy over the next two years. More massive black holes and discs have higher early uncertainty but higher luminosity at late times. The *HST* UV upper limit disfavours black holes with masses $\gtrsim 10^5\,M_\odot$, but does not strongly constrain discs around lower mass black holes. The *Swift* X-ray upper limit at $\sim$ 1 yr strongly disfavours these all of these plateau models, which suggests either a lower mass disc or black hole, or that AT2024wpp is not an IMBH TDE.

The late-time optical, UV, and X-ray upper limits can be used to exclude some regions of the M_{BH}–M_{disc} parameter space through modelling of the plateau emission in the case of an IMBH TDE – this is shown in Fig. 8 for all upper limits at >200 d, including limits from the VLT, HST, and *Swift*. We sample a log-uniform prior for both M_{BH} and M_{disc}, with M_{BH} ranging from 1–$10^5\,M_\odot$ and M_{disc} ranging from $0.05 - 10\,M_\odot$. The upper limit for the M_{BH} prior is because any larger black hole would cause the initial transient to be too slow, and the lower limit on disc mass prior was

Downloaded from academic.oup.com/mnras/article/550/1/stag1104/8705434 by Sarah Dakin user on 15 September 2026

chosen so we could examine tidal disruptions of the lowest mass stars. We calculate r_0 and $t_{\rm visc}$ using equations (1) and (2), and all other parameters use their default priors. Disc masses $\gtrsim 1\,{\rm M}_\odot$ are excluded with 99 per cent confidence for a black hole mass of $> 10^2\ {\rm M}_\odot$. At 90 per cent confidence, disc masses $\gtrsim 0.3\,{\rm M}_\odot$ are excluded for a black hole mass of $> 10^2\ {\rm M}_\odot$. Black hole masses of $\gtrsim 10^{4.5}$ and $\gtrsim 10^4\ {\rm M}_\odot$ are excluded for all disc masses at 99 per cent and 90 per cent confidence respectively. However, we caution against drawing too strong a conclusion from a posterior based only on a few upper limits.

5.2 Other scenarios

B. D. Metzger (2022a) outlined several progenitor scenarios for LFBOTs, including engine-powered SNe (e.g. S. J. Prentice et al. 2018), pulsational pair instability SNe (PPISNe, e.g. S.-C. Leung, J. Fuller & K. Nomoto 2021), prompt collapse from failed SNe or PPISNe (e.g. R. Margutti et al. 2019), IMBH TDEs (e.g. R. Margutti et al. 2019; D. A. Perley et al. 2019; E. Quataert et al. 2019), stellar mass BH TDEs (e.g. H. B. Perets et al. 2016; K. Kremer et al. 2019, 2023; P. Beniamini, H. B. Perets & J. Granot 2025), failed common envelope with a prompt merger (e.g. N. Soker 2019; N. Soker, A. Grichener & A. Gilkis 2019; S. L. Schrøder et al. 2020), and failed common envelope with a delayed merger (e.g. B. D. Metzger 2022a). This work examined engine-driven SNe and TDEs, while PPISNe and current failed common envelope models are not supported by the photospheric radius time-scales derived in Appendix B.

Failed SNe remain an intriguing possibility, though predicting their optical signatures is extremely challenging (E. R. Beasor et al. 2024), as theoretical models offer a wide range of predictions for what a failed SN might look like. Different models of failed SNe have predicted no observable signature (C. S. Kochanek et al. 2008), a long-lived infrared transient with little to no optical emission (E. Lovegrove & S. E. Woosley 2013), a long-lived optical transient (R. Perna et al. 2014), or even a short-lived relatively bright transient (A. Antoni & E. Quataert 2023; A. Antoni, Y.-F. Jiang & E. Quataert 2025), similar to an LFBOT. A. A. Chrimes et al. (2026) examine the possibility of failed SNe from very massive stars ($>30\,M_\odot$), similar to the progenitors of super-kilonovae (D. M. Siegel et al. 2022), and find that the rates, host metallicities, mass loss rates, and expected plateau emission roughly match with the LFBOT population and previous observations. In this case, LFBOTs may contribute significantly to r-process enrichment in galaxies.

Although there are no reliable models for the optical flare from a prompt collapse failed SN, the system should settle into an accretion disc at later times, similar to TDEs. The expected plateau emission for failed SNe involving high and low mass stars are shown in Fig. 9. The priors are similar to the IMBH TDE plateaus, except the initial disc radius r_0 is calculated by assuming the progenitor star is maximally rotating and the angular momentum of the black hole $J_{\rm BH}$ is much less than the angular momentum of the disc $J_{\rm disc}$. These assumptions give a radius

$$r_0 = 2R_\star \left(\frac{M_\star}{M_{\rm disc}}\right)^2 \left(\frac{M_\star}{M_{\rm BH}}\right), \tag{3}$$

with $M_\star = M_{\rm disc} + M_{\rm BH}$. It is worth noting that this calculation ignores the self-gravity of the disc, which can be important when $M_{\rm disc} \gtrsim M_{\rm BH}$. The F225W emission has ~3 mag of uncertainty and is fainter than the IMBH TDE plateau, and the observed upper limit is not constraining. The X-ray emission is predicted to be fainter than 10^{-2} mJy but have lots of uncertainty, except for the $M_{\rm disc} = M_{\rm BH} = 50\,{\rm M}_\odot$ case. The X-ray upper limit disfavours discs $\gtrsim 50\,{\rm M}_\odot$ but does not constrain black hole mass. Sampling the prior to find the excluded area in the failed SN scenario, as done with TDEs in Fig. 8, does not give meaningful constraints on either the black hole or disc mass.

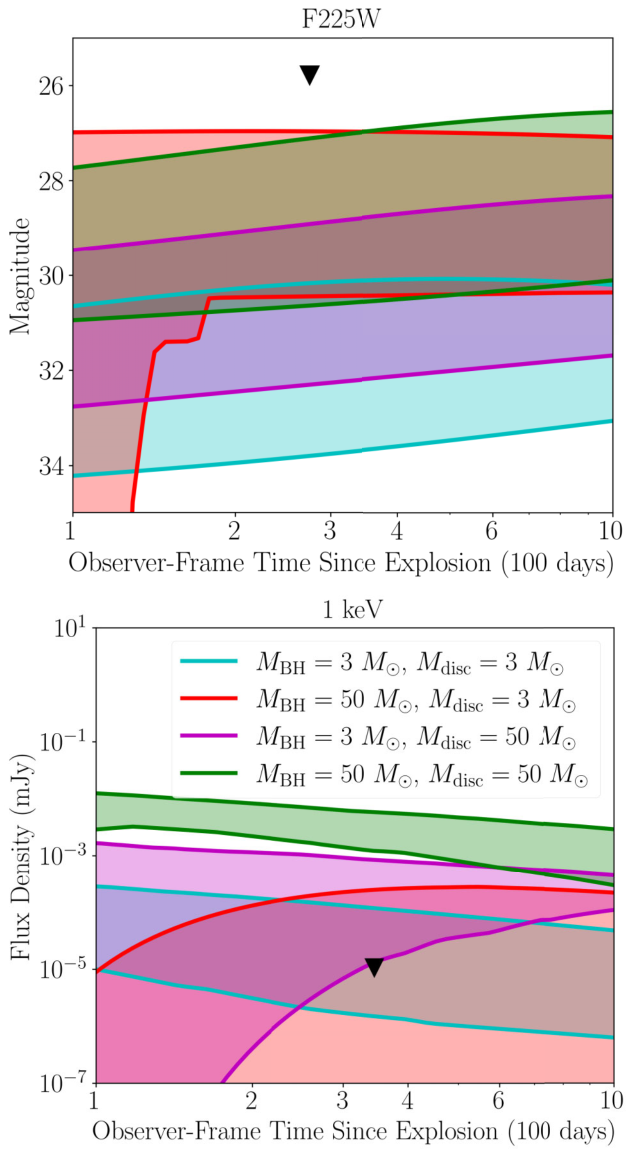

Figure 9. Same as Fig. 7, but for discs resulting from failed SNe.

Another scenario of interest is a reprocessing outflow, where an accretion disc powers an outflow that reprocesses the disc emission, powering an optical transient (A. L. Piro & W. Lu 2020; K. Uno & K. Maeda 2020a). Models of these outflows have successfully reproduced previous TDEs (K. Uno & K. Maeda 2020b; T. Matsumoto & T. Piran 2021) and LFBOTs (K. Uno & K. Maeda 2020a, 2023). The continuous mass injection of the model means that even though the outflow is expanding, the properties of the photospheric radius cannot be described by the relations in Appendix B. The photospheric radius will expand outward initially with the outflow until it reaches the radius where the outer region of the outflow is too diffuse to absorb light, and its recession is governed by the time-dependence of the mass outflow rate,

Downloaded from academic.oup.com/mnras/article/550/1/stag1104/8705434 by Sarah Dakin user on 15 September 2026

with the outflow becoming optically thin only when the outflow rate becomes sufficiently small. This should lead to an early photospheric peak and a late nebular phase, which is observed in AT2024wpp. Both A. L. Piro & W. Lu (2020) and K. Uno & K. Maeda (2023) predict an increase in photospheric temperature within the first 10 d post-explosion when the mass outflow rate and central luminosity are coupled, contrary to what is observed, but A. L. Piro & W. Lu (2020) show that the optical emission from AT2018cow can be reproduced if the central luminosity decreases faster than the mass outflow rate; they speculate that this could arise from either the X-rays being produced by a wind interacting with an equatorial torus which erodes over time, or from a viscously spreading disc causing the outflow velocity to decrease over time. A calculation of the X-ray opacity within this model would be useful to predict when the emission from the accretion disc will escape unattenuated.

5.3 Summary of previous interpretations

Our analysis of AT2024wpp and our interpretation of the event is mostly in broad agreement with previous studies. N. LeBaron et al. (2026) and D. A. Perley et al. (2026) both concluded that a homologously expanding medium can not explain the optical transient, and preferred a reprocessing outflow model similar to that discussed above, although no attempts were made to compare a model light curve to the data. O. Aspegren & D. Kasen (2026) reach a similar conclusion through simulations of line formation and suppression in LFBOT- and TDE-like transients. N. LeBaron et al. (2026) also discuss a dense CSM interaction model (D. K. Khatami & D. N. Kasen 2024) as well as BH–WR merger and TDE-powered SN models (B. D. Metzger 2022a; D. Tsuna & W. Lu 2025), ruling out the former but not the latter two.

The density profile and density from our modelling of the radio emission with a power-law synchrotron blast wave were $n_{\mathrm{CSM}} \propto r^{-2.9}$ and $n_{\mathrm{CSM}} \approx 10^7$ cm^{-3} at 10^{16} cm respectively, which match well with the shock modelling from A. J. Nayana et al. (2025) and D. A. Perley et al. (2026). Those works find that the shock radius recedes after $\sim$ 100 days, something which is not accounted for in any of our models and can explain the discrepancy at late times. They also both point out that these CSM properties seem to be typical of LFBOTs as well as some interacting SNe, such as the Type Ibn SN 2006jc (K. Maeda & T. J. Moriya 2022). This may imply similar progenitors for the two systems, as previously suggested by B. D. Metzger (2022a) and J. Klencki & B. D. Metzger (2025).

N. LeBaron et al. (2026) observe an excess of IR emission after $\sim$ 20–30 d, which was not well described by D. A. Perley et al. (2026) due to a lack of late-time IR observations. This excess is similar to the one observed in AT2018cow (R. Margutti et al. 2019; D. A. Perley et al. 2019), although it emerges at a later time-scale. Two models that can explain the IR excess are free–free opacity effects, which require several solar masses of outflow (C. Chen & R.-F. Shen 2022), and a dust echo (B. D. Metzger & D. A. Perley 2023), which reproduces the emission with densities similar to those inferred from the radio emission. As noted by N. LeBaron et al. (2026), this means the radio and IR emission can form in the same medium by completely separate processes.

A. J. Nayana et al. (2025) found that the X-ray rebrightening and spectral steepening can be explained by a Compton bump, and posit that the time-scale may be due to a drop in the X-ray opacity due to ionization breakout (B. D. Metzger & A. L. Piro 2014; B. D. Metzger et al. 2014) at $\sim$40 d. This also roughly corresponds to the time-scale at which the broad features disappear from the optical spectrum (D. A. Perley et al. 2026). The appearing and disappearing features are expected in a reprocessing outflow model, as the early medium should be hot and ionized until enough material has been expelled, then should remain partially ionized at the photosphere until the photosphere recedes into the ionized region (analogous to a Strömgren sphere) caused by the inner X-ray source. A. J. Nayana et al. (2025) favour a model with super-Eddington accretion onto a compact object which produces aspherical disc-wind outflows. The polarization measurements by M. Pursiainen et al. (2025) seem to prohibit large scale asymmetries in the outflow, although small-scale clumping can produce a polarization signal below the observed noise threshold (e.g. M. Tanaka et al. 2017).

Finally, D. A. Perley et al. (2026) used scaling relations (A. Mummery et al. 2024) to get a black hole mass constraint from the late-time non-detections of a plateau. They find a black hole mass limit of $3 \times 10^4 M_{\odot}$, similar to what we infer at 99 per cent confidence from Fig. 8.

6 SUMMARY AND CONCLUSIONS

In this work, we examined the optical, radio, and X-ray emission from the LFBOT AT2024wpp. The data were compared to a number of models to try and determine which physical scenario can best explain the transient. A few optical models, including the magnetar-powered SN model, SN + envelope and SN + CSM shock cooling models, and BH–WR merger model, can reproduce the optical data if the temperature of the model plateaus above 20 000 K. This is not unphysical but does imply that the ejecta should become optically thin on a much faster time-scale than what is suggested by the spectroscopic data (D. A. Perley et al. 2026). While GRB afterglow models and synchrotron blast wave models can explain the radio and X-ray emission separately, a combination of these models fails to adequately explain the non-thermal emission from the system.

Analysis of the behaviour of the photospheric radius disfavours models featuring a homologously expanding ejecta. Although the TDE models were not able to reproduce the data, we do not rule out this scenario due to the uncertainty of the emission mechanism in the stellar-mass/IMBH regime. The late-time optical emission from an accretion disc would likely be undetectable unless the black hole mass is almost supermassive, but X-rays may be detectable for the first several years. If the system is a TDE, current constraints favour the disruption of a low-mass star from a black hole with either intermediate or stellar mass.

AT2024wpp could be a failed SN with prompt black hole formation, but there are no reliable models for the optical flare in order to test the scenario. A failed SN would have an accretion disc that would also be detectable in X-rays and display different behaviour than accretion discs from IMBH TDEs, allowing the scenarios to be differentiated. A reprocessing wind may be able to explain the optical emission, and opacity calculations from that model would be useful for predicting late X-ray emission from the disc.

Downloaded from academic.oup.com/mnras/article/550/1/stag1104/8705434 by Sarah Dakin user on 15 September 2026

ACKNOWLEDGEMENTS

The authors would like to thank Kim Page for her help with *Swift* data, Ashley Chrimes and Christopher Irwin for helpful discussions, and the anonymous referee for their helpful comments. CMBO, GPL, and CT acknowledge support from the Royal Society (grant nos. DHF-R1-221175 and DHF-ERE-221005). NS acknowledges support from the Kavli Foundation. HH acknowledges support from the Japanese Society for the Promotion of Science Grant-in-Aid for Scientific Research (Grant nos. 26H00817 and 26K07147). ERB is supported by a Royal Society Dorothy Hodgkin Fellowship (grant no. DHF-R1-241114). NMK acknowledges support from LIV.INNO (Science and Technology Facilities Council grant ST/W006766/1).

DATA AVAILABILITY

All data used are publicly available from D. A. Perley et al. (2026). All models used are publicly available within REDBACK (N. Sarin et al. 2024).

REFERENCES

Adhyaqsa A., Malasan H. L., Aprilia, Puspitarini L., 2020, J. Phys. Conf. Ser., 1523, 012001
Alexander K. D. et al., 2026, ApJ, 1000, 139
Andreoni I. et al., 2022, Nature, 612, 430
Angus C. R., Levan A. J., Perley D. A., Tanvir N. R., Lyman J. D., Stanway E. R., Fruchter A. S., 2016, MNRAS, 458, 84
Angus C. R. et al., 2026, preprint (arXiv:2601.04406)
Antoni A., Quataert E., 2023, MNRAS, 525, 1229
Antoni A., Jiang Y.-F., Quataert E., 2025, preprint (arXiv:2509.16308)
Arcavi I. et al., 2016, ApJ, 819, 35
Arnett W. D., 1980, ApJ, 237, 541
Arnett W. D., 1982, ApJ, 253, 785
Arnett W. D., Fu A., 1989, ApJ, 340, 396
Ashton G. et al., 2019, ApJS, 241, 27
Aspegren O., Kasen D., 2026, ApJ, 1001, 191
Bade N., Komossa S., Dahlem M., 1996, A&A, 309, L35
Barlow M. J., Smith L. J., Willis A. J., 1981, MNRAS, 196, 101
Beasor E. R., Hosseinzadeh G., Smith N., Davies B., Jencson J. E., Pearson J., Sand D. J., 2024, ApJ, 964, 171
Bellm E. C. et al., 2019a, PASP, 131, 018002
Bellm E. C. et al., 2019b, PASP, 131, 018002
Beniamini P., Perets H. B., Granot J., 2026, Open J. Astrophys. 9, 57985
Blondin J. M., Chevalier R. A., 2017, ApJ, 845, 139
Bright J. S. et al., 2022, ApJ, 926, 112
Buchner J. et al., 2014, A&A, 564, A125
Calderón D., Pejcha O., Duffell P. C., 2021, MNRAS, 507, 1092
Chatzopoulos E. Wheeler J. C., Vinko J., Horvath Z. L., Nagy A., 2013, ApJ, 773, 76
Chen C., Shen R.-F., 2022, Res. Astron. Astrophys., 22, 035017
Chen T. W. et al., 2015, MNRAS, 452, 1567
Chen T.-W., Smartt S. J., Yates R. M., Nicholl M., Krühler T, Schady P., Dennefeld M., Inserra C., 2017, MNRAS, 470, 3566
Chen Y. et al., 2023a, ApJ, 955, 42
Chen Y., Drout M. R., Piro A. L. Kilpatrick C. D., Foley R. J., Rojas-Bravo C., Magee M. R., 2023b, ApJ, 955, 43
Chevalier R. A., Fransson C., 2017, in Alsabti A. W., Murdin P., eds, Handbook of Supernovae. Springer International Publishing, Berlin, p. 875
Chrimes A. A. et al., 2024a, MNRAS, 527, L47
Chrimes A. A., Coppejans D. L., Jonker P. G., Levan A. J., Groot P. J., Mummery M., Stanway E. R., 2024b, A&A, 691, A329
Chrimes A. A., Jonker P. G., Levan A. J., Mummery A., 2026, A&A, 706, A327
Colgate S. A., McKee C., 1969, ApJ, 157, 623
Coppejans D. L. et al., 2020, ApJ, 895, L23
Dekany R. et al., 2020, PASP, 132, 038001
Dessart L., Hillier D. J., Sukhbold T., Woosley S. E., Janka H.-T., 2021, A&A, 656, A61
Donley J. L., Brandt W. N., Eracleous M., Boller T., 2002, AJ, 124, 1308
Dou L., Wang T.-g., Jiang N., Yang C., Lyu J., Zhou H., 2016, ApJ, 832, 188
Drout M. R. et al., 2014, ApJ, 794, 23
DuPont M., MacFadyen A., Zrake J., 2022, ApJ, 931, L16
Fox O. D., Smith N., 2019, MNRAS, 488, 3772
Gal-Yam A., 2012, Science, 337, 927
Gomez S. et al., 2024, MNRAS, 535, 471
Gottlieb O., Tchekhovskoy A., Margutti R., 2022, MNRAS, 513, 3810
Graham M. J. et al., 2019, PASP, 131, 078001
Grotova I. et al., 2025, A&A, 697, A159
Guillochon J., Ramirez-Ruiz E., 2013, ApJ, 767, 25
Guillochon J., Nicholl M., Villar V. A., Mockler B., Narayan G., Mandel K. S., Berger E., Williams P. K. G., 2018, ApJS, 236, 6
Gutiérrez C. P. et al., 2024, ApJ, 977, 162
Hamidani H., Sato Y., Kashiyama K., Tanaka M., Ioka K., Kimura S. S., 2025a, ApJ, 986, L4
Hamidani H., Ioka K., Kashiyama K., Tanaka M., 2025b, ApJ, 988, 30
Hammerstein E. et al., 2023, ApJ, 942, 9
Ho A. Y. Q. et al., 2019, ApJ, 871, 73
Ho A. Y. Q. et al., 2020, ApJ, 895, 49
Ho A. Y. Q. et al., 2022, ApJ, 932, 116
Ho A. Y. Q. et al., 2023a, Nature, 623, 927
Ho A. Y. Q. et al., 2023b, ApJ, 949, 120
Ho A. Y. Q., Srinivasaragavan G., Perley D. et al., 2024, Transient Name Server AstroNote, 272, 1
Inkenhaag A., Jonker P. G., Levan A. J., Chrimes A. A., Mummery A., Perley D. A., Tanvir N. L., 2023, MNRAS, 525, 4042
Inkenhaag A., Levan A. J., Mummery A., Jonker P. G., 2025, MNRAS, 544, L108
Ji S., Wang Z., Zhu L., Geier S., Gupta A. C., 2025, ApJ, 991, 20
Jiang B., Jiang S., Ashley Villar V., 2020, Res. Notes Am. Astron. Soc., 4, 16
Jiang N., Zhou Z., Zhu J., Wang Y., Wang T., 2023, ApJ, 953, L12
Khatami D. K., Kasen D. N., 2024, ApJ, 972, 140
Klencki J., Metzger B. D., 2025, preprint (arXiv:2510.09745)
Kochanek C. S., Beacom J. F., Kistler M. D., Prieto J. L., 2008, ApJ, 684, 1336
Kremer K., Lu W., Rodriguez C. L. Rasio F. A., 2019, ApJ, 881, 75
Kremer K., Mockler B., Piro A. L., Lombardi J. C., 2023, MNRAS, 524, 6358
Kuin N. P. M. et al., 2019, MNRAS, 487, 2505
Lamb G. P., Mandel I., Resmi L., 2018, MNRAS, 481, 2581
Law C. J. et al., 2019, ApJ, 886, 24
LeBaron N. et al., 2026, ApJ, 997, L10
Leloudas G. et al., 2015, MNRAS, 449, 917
Leung S.-C., Fuller J., Nomoto K., 2021, ApJ, 915, 80
Li J.-Y. et al., 2025, ApJ, 992, 25
Liu J.-F., Zhu J.-P., Liu L.-D., Yu Y.-W., Zhang B., 2022, ApJ, 935, L34
Lovegrove E., Woosley S. E., 2013, ApJ, 769, 109
Lunnan R. et al., 2014, ApJ, 787, 138
Lyman J. D., Galbany L., Sánchez S. F., Anderson J. P., Kuncarayakti H., Prieto J. L., 2020, MNRAS, 495, 992
Lyutikov M., Toonen S., 2019, MNRAS, 487, 5618
Maeda K., Moriya T. J., 2022, ApJ, 927, 25
Margalit B., 2022, ApJ, 933, 238
Margalit B., Quataert E., 2021, ApJ, 923, L14
Margalit B., Quataert E., 2024, ApJ, 977, 134
Margutti R. et al., 2019, ApJ, 872, 18
Margutti R. et al., 2023, ApJ, 954, L45
Margutti R., J N. A., Chornock R. et al., 2024, Transient Name Server AstroNote, 339, 1
Masterson M. et al., 2024, ApJ, 961, 211
Matsumoto T., Piran T., 2021, MNRAS, 502, 3385

Downloaded from academic.oup.com/mnras/article/550/1/stag1104/8705434 by Sarah Dakin user on 15 September 2026

Matthews D. et al., 2023, Res. Notes Am. Astron. Soc., 7, 126
Maund J. R. et al., 2023, MNRAS, 521, 3323
Metzger B. D., 2022a, ApJ, 932, 84
Metzger B. D., 2022b, ApJ, 937, L12
Metzger B. D., Perley D. A., 2023, ApJ, 944, 74
Metzger B. D., Piro A. L., 2014, MNRAS, 439, 3916
Metzger B. D., Vurm I., Hascoët R., Beloborodov A. M., 2014, MNRAS, 437, 703
Michałowski M. J. et al., 2019, A&A, 627, A106
Migliori G. et al., 2024, ApJ, 963, L24
Mockler B., Guillochon J., Ramirez-Ruiz E., 2019, ApJ, 872, 151
Mummery A., Balbus S. A., 2020, MNRAS, 492, 5655
Mummery A., van Velzen S., Nathan E., Ingram A., Hammerstein E., Fraser-Taliente L., Balbus S., 2024, MNRAS, 527, 2452
Mummery A., Nathan E., Ingram A., Gardner M., 2025, MNRAS, 544, 2225
Nayana A. J., Chandra P., 2021, ApJ, 912, L9
Nayana A. J. et al., 2025, ApJ, 993, L6
Newsome M. et al., 2024, ApJ, 961, 239
Nicholl M., 2021, Astron. Geophys., 62, 5
Nicholl M., Guillochon J., Berger E., 2017, ApJ, 850, 55
Nugis T., Lamers H. J. G. L. M., 2000, A&A, 360, 227
Ofek E. O. et al., 2025, ApJ, 993, 76
Omand C. M. B., Jerkstrand A., 2023, A&A, 673, A107
Omand C. M. B., Sarin N., 2024, MNRAS, 527, 6455
Omand C. M. B., Kashiyama K., Murase K., 2018, MNRAS, 474, 573
Omand C. M. B., Kashiyama K., Murase K., 2019, MNRAS, 484, 5468
Omand C. M. B., Sarin N., Temim T., 2025a, MNRAS, 536, 408
Omand C. M. B., Sarin N., Lamb G. P., 2025b, MNRAS, 539, 1908
Ørum S. V. et al., 2020, A&A, 643, A47
Pasham D. R. et al., 2021, Nat. Astron., 6, 249
Pellegrino C. et al., 2022, ApJ, 926, 125
Perets H. B., Li Z., Lombardi J. C., Jr, Milcarek S R. Jr., 2016, ApJ, 823, 113
Perley D. A. et al., 2019, MNRAS, 484, 1031
Perley D. A. et al., 2021, MNRAS, 508, 5138
Perley D. A., Qin Y., Rich R. M. et al., 2024, Transient Name Server AstroNote, 280, 1
Perley D. A. et al., 2026, MNRAS,549,30
Perna R., Duffell P., Cantiello M., MacFadyen A. I., 2014, ApJ, 781, 119
Piran T., Svirski G., Krolik J., Cheng R. M., Shiokawa H., 2015, ApJ, 806, 164
Piro A. L., Kollmeier J. A., 2018, ApJ, 855, 103
Piro A. L., Lu W., 2020, ApJ, 894, 2
Piro A. L., Haynie A., Yao Y., 2021, ApJ, 909, 209
Prentice S. J. et al., 2018, ApJ, 865, L3
Pursiainen M. et al., 2018, MNRAS, 481, 894
Pursiainen M. et al., 2025, MNRAS, 537, 3298
Quataert E., Lecoanet D., Coughlin E. R., 2019, MNRAS, 485, L83
Rivera Sandoval L. E., Maccarone T. J., Corsi A., Brown P. J., Pooley D., Wheeler J. C., 2018, MNRAS, 480, L146
Rosswog S., Brüggen M., 2007, Introduction to High-Energy Astrophysics, Cambridge University Press, New York, p. 101
Ryu T., Krolik J., Piran T., 2020, ApJ, 904, 73
Sapir N., Waxman E., 2017, ApJ, 838, 130
Sarin N., Metzger B. D., 2024, ApJ, 961, L19
Sarin N., Omand C. M. B., Margalit B., Jones D. I., 2022, MNRAS, 516, 4949
Sarin N. et al., 2024, MNRAS, 531, 1203
Schrøder S. L., MacLeod M., Loeb A., Vigna-Gómez A., Mandel I., 2020, ApJ, 892, 13
Schroeder G., Ho A. Y. Q., Perley D. A., 2024, Transient Name Server AstroNote, 314, 1
Schulze S. et al., 2018, MNRAS, 473, 1258
Schulze S. et al., 2024, A&A, 683, A223
Siegel D. M., Agarwal A., Barnes J., Metzger B. D., Renzo M., Villar V. A., 2022, ApJ, 941, 100
Sądowski A., Narayan R., 2015, MNRAS, 453, 3213
Smith P. S., Leonard D. C., Bilinski C. et al., 2018, Astron. Telegram, 11789, 1
Soker N., 2019, Sci. China Phys. Mech. Astron., 62, 119501
Soker N., 2022, Res. Astron. Astrophys., 22, 055010
Soker N., Grichener A., Gilkis A., 2019, MNRAS, 484, 4972
Somalwar J. J. et al., 2025, ApJ, 995, 228
Srinivasaragavan G., Ho A., Perley D. et al., 2024, Transient Name Server AstroNote, 276, 1
Stein R. et al., 2021, Nat. Astron., 5, 510
Sun N.-C., Maund J. R., Crowther P. A., Liu L.-D., 2022, MNRAS, 512, L66
Sun N.-C., Maund J. R., Shao Y. ,Janiak I. A., 2023, MNRAS, 519, 3785
Suzuki A., Maeda K., 2017, MNRAS, 466, 2633
Suzuki A., Maeda K., 2021, ApJ, 908, 217
Suzuki A., Maeda K., 2022, ApJ, 925, 148
Suzuki A., Irwin C. M., Maeda K., 2024, PASJ, 76, 863
Taddia F. et al., 2019, A&A, 621, A71
Tanaka M., Maeda K., Mazzali P. A., Kawabata K. S., Nomoto K., 2017, ApJ, 837, 105
Tonry J. L., 2011, PASP, 123, 58
Tonry J. L. et al., 2018, PASP, 130, 064505
Toshikage S., Kimura S. S., Shimizu N., Tanaka M., Yoshida S., Iwakiri W. B., Morokuma T., 2025, ApJ, 993, 23
Tsuna D., Lu W., 2025, ApJ, 986, 84
Uno K., Maeda K., 2020a, ApJ, 897, 156
Uno K., Maeda K., 2020b, ApJ, 905, L5
Uno K., Maeda K., 2023, MNRAS, 521, 4598
van Velzen S. et al., 2016, Science, 351, 62
Villar V. A., Berger E., Metzger B. D., Guillochon J, 2017, ApJ, 849, 70
Vurm I., Metzger B. D., 2021, ApJ, 917, 77
Wise J. L. et al., 2026, MNRAS, 546, stag130
Xiang D. et al., 2021, ApJ, 910, 42
Yao Y. et al., 2022, ApJ, 934, 104
Zauderer B. A. et al., 2011, Nature, 476, 425

APPENDIX A: PRIORS AND SUMMARY STATISTICS

Tables A1-A20 show the priors and posterior summary statistics for the fits shown in Figs 2, 3, 4, and 6.

Downloaded from academic.oup.com/mnras/article/550/1/stag1104/8705434 by Sarah Dakin user on 15 September 2026

Table A1. Priors and summary statistics for the ^{56}Ni-powered supernova supernova models in Figs 2 and 3. Priors are either uniform (U) or log-uniform (L). The values shown for the posterior are the median and 1σ uncertainties. Posterior values denoted with L are given in log-space.

Parameter	Symbol	Units	Prior	Posterior Fig. 2	Posterior Fig. 3
Ejecta mass	M_{ej}	$M_\odot$	$L[10^{-4}, 10^2]$	8.83 ± 0.07	4.87 ± 0.00
Ejecta velocity	v_{ej}	km s^{-1}	$L[10^3, 10^5]$	$L(5 \pm 0.00)$	$L(4.99 \pm 0.00)$
Nickel fraction	f_{Ni}		$L[10^{-3}, 1]$	1.00 ± 0.00	1.00 ± 0.00
Opacity	κ	cm^2 g^{-1}	$U[0.05, 2]$	0.05 ± 0.00	0.05 ± 0.00
Non-thermal opacity	κ_γ	cm^2 g^{-1}	$L[10^{-4}, 10^4]$	0.01 ± 0.00	0.02 ± 0.00
Plateau temperature	T_{floor}	K	$L[10^3, 10^5]$ (Fig. 2)	15110 ± 40	
			$L[10^3, 10^4]$ (Fig. 3)		9998.9 ± 0.1

Table A2. Same as Table A1, but for the magnetar-powered supernova model.

Parameter	Symbol	Units	Prior	Posterior Fig. 2	Posterior Fig. 3
Ejecta mass	M_{ej}	$M_\odot$	$L[10^{-1}, 10^2]$	$0.40^{+0.00}_{-0.01}$	0.26 ± 0.00
Explosion energy	E_{SN}	erg	$U[5 \times 10^{50}, 2 \times 10^{51}]$	$L(50.72^{+0.03}_{-0.02})$	$L(50.70 \pm 0.00)$
Nickel fraction	f_{Ni}		$L[10^{-4}, 1]$	$L(-0.62 \pm 0.03)$	$L(-1.26 \pm 0.02)$
Opacity	κ	cm^2 g^{-1}	$U[0.05, 0.2]$	0.05 ± 0.00	0.05 ± 0.00
Non-thermal opacity	κ_γ	cm^2 g^{-1}	$L[10^{-4}, 10^4]$	0.012 ± 0.00	0.001 ± 0.000
Initial magnetar luminosity	L_0	erg s^{-1}	$L[10^{40}, 10^{50}]$	$L(46.74^{+0.02}_{-0.04})$	$L(45.73 \pm 0.01)$
Spin-down time-scale	t_{SD}	s	$L[10^2, 10^8]$	$L(4.74 \pm 0.03)$	$L(5.71 \pm 0.02)$
Braking Index	n		$U[1.5, 10]$	$4.06^{+0.09}_{-0.10}$	$9.80^{+0.15}_{-0.30}$
Plateau temperature	T_{floor}	K	$L[10^3, 10^5]$ (Fig. 2)	47900 ± 200	
			$L[10^3, 10^4]$ (Fig. 3)		9999 ± 1

Table A3. Same as Table A1, but for the CSM-powered supernova model.

Parameter	Symbol	Units	Prior	Posterior Fig. 2	Posterior Fig. 3
Ejecta mass	M_{ej}	$M_\odot$	$L[10^{-4}, 10^2]$	0.0001 ± 0.0000	1.47 ± 0.00
Explosion energy	E_{SN}	erg	$L[10^{48}, 10^{52}]$	$L(50.46 \pm 0.00)$	$L(52.00 \pm 0.00)$
Nickel fraction	f_{Ni}		$L[10^{-3}, 1]$	$L(-1.50^{+1.04}_{-1.03})$	$0.99^{+0.01}_{-0.02}$
Opacity	κ	cm^2 g^{-1}	$U[0.05, 2]$	1.99 ± 0.00	0.05 ± 0.00
Non-thermal opacity	κ_γ	cm^2 g^{-1}	$L[10^{-4}, 10^4]$	$L(-0.01^{+2.72}_{-2.75})$	0.01 ± 0.00
CSM mass	M_{CSM}	$M_\odot$	$L[10^{-4}, 10^2]$	0.46 ± 0.00	1.28 ± 0.00
CSM density profile index	η		$U[0, 2]$	0.97 ± 0.01	2.00 ± 0.00
CSM density	ρ	cm^{-3}	$L[10^{-15}, 10^{-12}]$	$L(-14.64 \pm 0.01)$	$L(-12.76 \pm 0.00)$
CSM shell radius	r_0	AU	$U[50, 700]$	50.0 ± 0.1	63.0 ± 0.1
Plateau temperature	T_{floor}	K	$L[10^3, 10^5]$ (Fig. 2)	99972^{+21}_{-44}	
			$L[10^3, 10^4]$ (Fig. 3)		10000^{+0}_{-1}

Table A4. Same as Table A1, but for the fallback-powered supernova model.

Parameter	Symbol	Units	Prior	Posterior Fig. 2	Posterior Fig. 3
Ejecta mass	M_{ej}	$M_\odot$	$L[10^{-4}, 10^2]$	$L(-2.7^{+1.2}_{-0.9})$	$L(-3.2^{+0.9}_{-0.5})$
Ejecta velocity	v_{ej}	km s^{-1}	$L[10^3, 10^5]$	$L(4.62 \pm 0.00)$	$L(4.78 \pm 0.00)$
Nickel fraction	f_{Ni}		$L[10^{-3}, 1]$	$L(-1.92^{+1.07}_{-0.75})$	$L(-2.23^{+0.85}_{-0.54})$
Opacity	κ	cm^2 g^{-1}	$U[0.05, 2]$	1.03 ± 0.64	1.03 ± 0.65
Non-thermal opacity	κ_γ	cm^2 g^{-1}	$L[10^{-4}, 10^4]$	$0.97^{+427.33}_{-0.97}$	$0.69^{+392.57}_{-0.69}$
Fallback luminosity	L_1	erg s^{-1}	$L[10^{51}, 10^{57}]$	$L(56.03^{+0.00}_{-0.01})$	$L(53.53 \pm 0.00)$
Fallback transition time	t_{tr}	d	$L[10^{-4}, 10^2]$	$2.36^{+0.04}_{-0.05}$	2.16 ± 0.03
Plateau temperature	T_{floor}	K	$L[10^3, 10^5]$ (Fig. 2)	99700^{+200}_{-500}	
			$L[10^3, 10^4]$ (Fig. 3)		2230 ± 10

Downloaded from academic.oup.com/mnras/article/550/1/stag1104/8705434 by Sarah Dakin user on 15 September 2026

Table A5. Same as Table A1, but for the SN + envelope shock cooling model.

Parameter	Symbol	Units	Prior	Posterior Fig. 2	Posterior Fig. 3
Ejecta mass	M_{ej}	$M_\odot$	L[10^{-4}, 10^2]	12.5 ± 0.4	$91.3^{+1.1}_{-0.8}$
Shock velocity	v_{sh}	km s^{-1}	L[10^3, 5×10^4]	L(4.59 ± 0.00)	L(4.61 ± 0.00)
Nickel fraction	f_{Ni}		L[10^{-3}, 1]	1.00 ± 0.00	0.001 ± 0.000
Opacity	κ	cm^2 g^{-1}	U[0.01, 1]	0.01 ± 0.00	0.01 ± 0.00
Non-thermal opacity	κ_γ	cm^2 g^{-1}	L[10^{-4}, 10^4]	L(-2.88 ± 0.03)	L(-2.78 ± 0.01)
Envelope mass	M_{env}	$M_\odot$	L[10^{-3}, 5]	1.45 ± 0.03	0.38 ± 0.00
Envelope structure coefficient	f_ρ		U[0.5, 3]	$2.88^{+0.09}_{-0.18}$	$1.62^{+0.01}_{-0.02}$
Stellar radius	R_*	10^{13} cm	L[10^{-3}, 10]	5.62 ± 0.18	3.88 ± 0.01
Plateau temperature	T_{floor}	K	L[10^3, 10^5] (Fig. 2)	31500 ± 300	
			L[10^3, 10^4] (Fig. 3)		9988^{+2}_{-2}

Table A6. Same as Table A1, but for the SN + CSM shock cooling model.

Parameter	Symbol	Units	Prior	Posterior Fig. 2	Posterior Fig. 3
Ejecta mass	M_{ej}	$M_\odot$	L[10^{-4}, 10^2]	$9.11^{+0.00}_{-0.01}$	$1.43^{+0.03}_{-0.05}$
Ejecta velocity	v_{ej}	km s^{-1}	L[10^3, 10^5]	L(4.92 ± 0.00)	L(4.66 ± 0.00)
Nickel fraction	f_{Ni}		L[10^{-3}, 1]	1.00 ± 0.00	0.97 ± 0.01
Opacity	κ	cm^2 g^{-1}	U[0.05, 2]	0.05 ± 0.00	0.32 ± 0.00
Non-thermal opacity	κ_γ	cm^2 g^{-1}	L[10^{-4}, 10^4]	0.01 ± 0.00	0.04 ± 0.00
CSM mass	M_{CSM}	$M_\odot$	L[10^{-2}, 10^3]	L(0.10 ± 0.00)	L(-0.06 ± 0.01)
CSM radius	R_{CSM}	10^{13} cm	L[10^{-3}, 10]	8.86 ± 0.01	10.00 ± 0.00
CSM energy	E_{CSM}	erg	L[10^{40}, 10^{52}]	L(51.98 ± 0.00)	L(51.96 ± 0.00)
Inner density index	δ		U[1, 1.5]	1.2 ± 0.00	$1.12^{+0.06}_{-0.05}$
Outer density index	n		U[8, 12]	10.86 ± 0.01	8.78 ± 0.01
Plateau temperature	T_{floor}	K	L[10^3, 10^5] (Fig. 2)	18492^{+4}_{-5}	
			L[10^3, 10^4] (Fig. 3)		9988^{+7}_{-9}

Table A7. Same as Table A1, but for the cocoon + envelope shock cooling model.

Parameter	Symbol	Units	Prior	Posterior Fig. 2	Posterior Fig. 3
Ejecta mass	M_{ej}	$M_\odot$	L[10^{-1}, 10^2]	$9.72^{+0.09}_{-0.20}$	$2.31^{+0.02}_{-0.03}$
Ejecta velocity	v_{ej}	km s^{-1}	L[10^3, 10^5]	L(5.00 ± 0.00)	L(4.37 ± 0.00)
Nickel fraction	f_{Ni}		L[10^{-3}, 1]	1.00 ± 0.00	1.00 ± 0.00
Opacity	κ	cm^2 g^{-1}	U[0.05, 2]	0.05 ± 0.00	0.05 ± 0.00
Non-thermal opacity	κ_γ	cm^2 g^{-1}	L[10^{-4}, 10^4]	0.01 ± 0.00	0.0038 ± 0.0001
Cocoon mass	M_{coc}	$M_\odot$	U[0.1, 2]	1.60 ± 0.04	1.52 ± 0.02
Cocoon velocity	v_{coc}	c	U[0.01, 0.3]	0.15 ± 0.00	0.16 ± 0.00
Cocoon density index	η		U[1, 5]	4.97 ± 0.01	4.96 ± 0.03
Shock breakout time	t_{SBO}	s	U[0.1, 100]	$98.5^{+0.6}_{-0.7}$	99.9 ± 0.01
Shocked fraction of cocoon	f_{sh}		U[0.01, 1]	0.65 ± 0.02	0.90 ± 0.01
Cocoon opening angle	$\cos(\theta_{coc})$		U[0.866, 1]	0.87 ± 0.00	0.866 ± 0.000
Plateau temperature	T_{floor}	K	L[10^3, 10^5] (Fig. 2)	19980^{+90}_{-110}	
			L[10^3, 10^4] (Fig. 3)		8930 ± 10

Downloaded from academic.oup.com/mnras/article/550/1/stag1104/8705434 by Sarah Dakin user on 15 September 2026

Table A8. Same as Table A1, but for the cocoon + CSM shock cooling model.

Parameter	Symbol	Units	Prior	Posterior Fig. 2	Posterior Fig. 3
Ejecta mass	$M_{\rm ej}$	$M_\odot$	$L[10^{-1}, 10^2]$	14.3 ± 0.2	$1.16^{+0.00}_{-0.01}$
Ejecta velocity	$v_{\rm ej}$	km s^{-1}	$L[10^3, 10^5]$	99100 ± 400	4120 ± 20
Nickel fraction	$f_{\rm Ni}$		$L[10^{-3}, 1]$	1.00 ± 0.00	0.91 ± 0.00
Opacity	κ	cm^2 g^{-1}	U[0.05, 2]	0.050 ± 0.000	0.050 ± 0.000
Non-thermal opacity	κ_γ	cm^2 g^{-1}	$L[10^{-4}, 10^4]$	$0.0046^{+0.0002}_{-0.0001}$	0.0005 ± 0.0000
Engine energy	$E_{\rm eng}$	erg	$L[10^{48}, 10^{53}]$	$L(51.62 \pm 0.01)$	$L(51.84 \pm 0.00)$
Engine time-scale	$t_{\rm eng}$	s	$L[1, 10^4]$	120^{+20}_{-10}	410^{+50}_{-20}
Cocoon opening angle	$\theta_{\rm coc}$	rad	U[0.01, 0.1]	0.011 ± 0.001	0.070 ± 0.001
CSM mass	$M_{\rm CSM}$	$M_\odot$	$L[10^{-2}, 10]$	0.94 ± 0.01	1.413 ± 0.001
CSM radius	$R_{\rm CSM}$	10^{13} cm	$L[10^{-2}, 10^2]$	10.3 ± 0.2	12.0 ± 0.0
Plateau temperature	$T_{\rm floor}$	K	$L[10^3, 10^5]$ (Fig. 2)	19960^{+70}_{-50}	
			$L[10^3, 10^4]$ (Fig. 3)		9930 ± 10

Table A9. Same as Table A1, but for the fallback TDE model.

Parameter	Symbol	Units	Prior	Posterior
Black hole mass	$M_{\rm BH}$	$10^6 M_\odot$	$L[10^{-6}, 1]$	1.00 ± 0.00
Stellar mass	M_*	$M_\odot$	L[0.05, 10]	$9.99^{+0.01}_{-0.02}$
Viscous time-scale	$t_{\rm visc}$	d	$L[10^{-3}, 10^2]$	4.23 ± 0.07
Scaled impact parameter	b		U[0, 2]	0.32 ± 0.00
Efficiency	η		$L[10^{-4}, 0.4]$	$L(-3.00 \pm 0.00)$
Photosphere power-law constant	$R_{\rm ph,0}$	cm	$L[10^{-4}, 10^4]$	53.4 ± 0.9
Photosphere power-law exponent	l		U[0, 2]	2.00 ± 0.00

Table A10. Same as Table A1, but for the stream-stream TDE model.

Parameter	Symbol	Units	Prior	Posterior
Black hole mass	$M_{\rm BH}$	$10^6 M_\odot$	$L[10^{-6}, 1]$	$0.10^{+0.16}_{-0.06}$
Stellar mass	M_*	$M_\odot$	U[0.05, 10]	$5.96^{+2.46}_{-2.96}$
Gaussian peak time	$t_{\rm peak}$	d	U[0, 60]	$45.86^{+8.60}_{-10.38}$
Gaussian sharpness	σ_t	d	U[0, 60]	$0.44^{+0.35}_{-0.28}$

Table A11. Same as Table A1, but for the cooling envelope TDE model.

Parameter	Symbol	Units	Prior	Posterior
Black hole mass	$M_{\rm BH}$	$M_\odot$	$L[1, 10^6]$	296^{+1}_{-2}
Stellar mass	M_*	$M_\odot$	L[0.05, 10]	10.00 ± 0.00
Impact parameter	β		U[1, 100]	86 ± 4
Viscosity parameter	α		L[0.1, 1]	$0.50^{+0.33}_{-0.30}$
Feedback efficiency	η		$L[10^{-4}, 0.1]$	$L(-1.85^{+0.40}_{-0.42})$
Gaussian peak time	$t_{\rm peak}$	d	U[5, 60]	1.57 ± 0.00
Gaussian sharpness	σ_t	d	U[5, 60]	0.037 ± 0.000

Downloaded from academic.oup.com/mnras/article/550/1/stag1104/8705434 by Sarah Dakin user on 15 September 2026

Table A12. Same as Table A1, but for the WR + BH merger model.

Parameter	Symbol	Units	Prior	Posterior	
				Fig. 2	Fig. 3
Stellar mass	M_*	$M_\odot$	U[5, 50]	46^{+3}_{-4}	$50.0^{+0.0}_{-0.1}$
Black hole mass	M_{BH}	$M_\odot$	U[5, 50]	$6.1^{+1.2}_{-0.8}$	$50.0^{+0.0}_{-0.1}$
CSM mass	M_{CSM}	$M_\odot$	U[0.1, 5]	$1.40^{+0.25}_{-0.15}$	0.40 ± 0.04
Fast component mass	M_{fast}	$M_\odot$	U[0.01, 1]	1.00 ± 0.00	0.088 ± 0.001
Fast component velocity	v_{fast}	c	U[0.05, 0.3]	0.21 ± 0.00	0.094 ± 0.00
Slow component velocity	v_{slow}	km s^{-1}	L[10^3, 10^4]	6300 ± 600	4000 ± 300
Viscosity parameter	α		L[0.1, 1]	0.11 ± 0.01	0.210 ± 0.001
Feedback efficiency	η		L[10^{-4}, 0.1]	0.069 ± 0.09	0.10 ± 0.00
Plateau temperature	T_{floor}	K	L[10^3, 10^5] (Fig. 2)	28100^{+200}_{-100}	
			L[10^3, 10^4] (Fig. 3)		9999 ± 1

Table A13. Priors and summary statistics for the radio and X-ray top-hat jet afterglow models in Fig. 4. Priors are either uniform (U) or log-uniform (L). The values shown for the posterior are the median and 1σ uncertainties. Posterior values denoted with L are given in log-space.

Parameter	Symbol	Units	Prior	Posterior	
				Radio	X-ray
Observer angle	θ_{ob}	rad	Sine[0, $\pi/2$]	$0.187^{+0.000}_{-0.001}$	$0.28^{+0.07}_{-0.06}$
Jet opening angle	θ_c	rad	U[0.01, 0.1]	0.028 ± 0.001	$0.075^{+0.017}_{-0.020}$
Isotropic equivalent jet energy	E_{jet}	erg	L[10^{44}, 10^{54}]	L($53.0^{+0.3}_{-0.4}$)	L($52.4^{+0.9}_{-0.6}$)
ISM density	n_0	cm^{-3}	L[10^{-5}, 10^2]	L($-2.3^{+0.3}_{-0.4}$)	L($1.1^{+0.5}_{-0.9}$)
Electron spectral index	p		U[2, 3]	2.13 ± 0.03	$2.32^{+0.31}_{-0.16}$
Particle equipartition parameter	ϵ_e		L[10^{-5}, 1]	L(-0.33 ± 0.20)	L($-0.69^{+0.44}_{-0.69}$)
Magnetic field equipartition parameter	ϵ_B		L[10^{-5}, 1]	L(-1.5 ± 1.0)	L($-1.9^{+1.2}_{-1.4}$)
Initial Lorentz factor	Γ_0		U[100,2000]	160^{+250}_{-50}	1000^{+600}_{-500}
Accelerated electron fraction	ξ_N		U[0,1]	$0.79^{+0.13}_{-0.16}$	0.51 ± 0.30

Table A14. Same as Table A13, but for the radio and X-ray gaussian jet afterglow models.

Parameter	Symbol	Units	Prior	Posterior	
				Radio	X-ray
Observer angle	θ_{ob}	rad	Sine[0, $\pi/2$]	0.88 ± 0.00	$0.35^{+0.06}_{-0.07}$
Jet core angle	θ_c	rad	U[0.01, 0.1]	0.010 ± 0.000	$0.056^{+0.024}_{-0.019}$
Jet edge angle	θ_j	rad	U[0.1, 0.2]	0.10 ± 0.00	$0.14^{+0.04}_{-0.02}$
Isotropic equivalent jet energy	E_{jet}	erg	L[10^{44}, 10^{54}]	L(52.97 ± 0.01)	L($52.3^{+0.7}_{-0.4}$)
ISM density	n_0	cm^{-3}	L[10^{-5}, 10^2]	L(2.00 ± 0.00)	L($1.4^{+0.4}_{-0.7}$)
Electron spectral index	p		U[2, 3]	$2.38^{+0.01}_{-0.02}$	$2.35^{+0.29}_{-0.19}$
Particle equipartition parameter	ϵ_e		L[10^{-5}, 1]	L($-0.96^{+0.01}_{-0.02}$)	L($-0.45^{+0.29}_{-0.46}$)
Magnetic field equipartition parameter	ϵ_B		L[10^{-5}, 1]	L(-0.75 ± 0.02)	L($-1.9^{+1.2}_{-1.4}$)
Initial Lorentz factor	Γ_0		U[100,2000]	1400^{+400}_{-500}	1100^{+500}_{-600}
Accelerated electron fraction	ξ_N		U[0,1]	$1.00^{+0.00}_{-0.01}$	$0.54^{+0.29}_{-0.33}$

Table A15. Same as Table A13, but for the radio and X-ray power-law synchrotron blast wave models.

Parameter	Symbol	Units	Prior	Posterior	
				Radio	X-ray
Shock velocity	v_{shock}	km s^{-1}	U[10^3, 3×10^4]	29700^{+200}_{-300}	18000^{+8000}_{-9000}
CSM density at 10^{15} cm	A	cm^{-3}	L[10^{-5}, 10^{15}]	L(9.63 ± 0.06)	L(9.1 ± 1.3)
CSM density index	s		U[0,4]	2.86 ± 0.01	2.06 ± 0.11
Electron spectral index	p		U[2, 3]	2.34 ± 0.03	$2.4^{+0.4}_{-0.3}$
Particle equipartition parameter	ϵ_e		L[10^{-5}, 1]	L($-0.07^{+0.05}_{-0.07}$)	L(-2.5 ± 1.7)
Magnetic field equipartition parameter	ϵ_B		L[10^{-5}, 1]	L($-4.94^{+0.08}_{-0.04}$)	L($-2.6^{+1.7}_{-1.5}$)

Downloaded from academic.oup.com/mnras/article/550/1/stag1104/8705434 by Sarah Dakin user on 15 September 2026

Table A16. Same as Table A13, but for the radio and X-ray thermal synchrotron blast wave models.

Parameter	Symbol	Units	Prior	Posterior	
				Radio	X-ray
Shock velocity	$\beta\Gamma$		U[0.1, 10]	0.13 ± 0.01	1.5 ± 0.7
ISM density	$n_{\rm ISM}$	$\rm cm^{-3}$	U[0, 10]	$3.5^{+3.7}_{-2.6}$	$4.4^{+3.2}_{-2.9}$
Mass loss parameter	$\dot{M} v_{\rm wind}$	$\rm M_{\odot}\ s\ km^{-1}\ yr^{-1}$	$\rm L[10^{-10}, 1]$	$\rm L(-5.8^{+0.3}_{-0.5})$	$\rm L(-5.7^{+0.6}_{-0.7})$
Electron spectral index	p		U[2, 3]	2.02 ± 0.01	$2.94^{+0.04}_{-0.09}$
Particle equipartition parameter	ϵ_e		$\rm L[10^{-5}, 1]$	$\rm L(-1.7^{+0.5}_{-0.7})$	$\rm L(-3.0^{+1.8}_{-1.3})$
Magnetic field equipartition parameter	ϵ_B		$\rm L[10^{-5}, 1]$	$\rm L(-4.4 \pm 0.4)$	$\rm L(-2.6^{+1.7}_{-1.6})$
Accelerated electron fraction	ξ_N		U[0,1]	$0.64^{+0.20}_{-0.26}$	$0.54^{+0.28}_{-0.29}$

Table A17. Same as Table A13, but for the X-ray accretion disc model.

Parameter	Symbol	Units	Prior	Posterior
Black hole mass	$M_{\rm BH}$	$\rm M_{\odot}$	$\rm L[1, 10^{10}]$	$\rm L(5.6^{+1.2}_{-0.7})$
Black hole spin	a		U[−1, 1]	$-0.48^{+0.50}_{-0.32}$
Disc mass	$M_{\rm disc}$	$\rm M_{\odot}$	$\rm L[10^{-3}, 10]$	$\rm L(-2.02^{+1.94}_{-0.61})$
Initial radius of disc	R_0	$R_{\rm grav}$	U[10, 100]	79^{+12}_{-19}
Viscous time-scale	$t_{\rm visc}$	day	$\rm L[1, 10^3]$	$4.2^{+5.7}_{-2.4}$
Time of ring formation	$t_{\rm form}$	day	U[−100, 365]	$12.8^{+9.3}_{-6.1}$
Observer angle	$\theta_{\rm obs}$	rad	Sine[0, $\pi/2$]	$0.88^{+0.37}_{-0.33}$

Table A18. Same as Table A13, but for the X-ray top-hat jet afterglow + accretion disc model.

Parameter	Symbol	Units	Prior	Posterior
Black hole mass	$M_{\rm BH}$	$\rm M_{\odot}$	$\rm L[1, 10^{10}]$	$\rm L(5.3^{+0.4}_{-0.5})$
Black hole spin	a		U[−1, 1]	$-0.43^{+0.40}_{-0.33}$
Disc mass	$M_{\rm disc}$	$\rm M_{\odot}$	$\rm L[10^{-3}, 10]$	$0.004^{+0.010}_{-0.002}$
Initial radius of disc	R_0	$R_{\rm grav}$	U[10, 100]	43^{+25}_{-19}
Viscous time-scale	$t_{\rm visc}$	d	$\rm L[1, 10^3]$	$4.9^{+6.0}_{-2.6}$
Time of ring formation	$t_{\rm form}$	d	U[−100, 365]	$11.1^{+4.9}_{-3.4}$
Observer angle	$\theta_{\rm ob}$	rad	Sine[0, $\pi/2$]	$1.25^{+0.19}_{-0.32}$
Isotropic equivalent jet energy	$E_{\rm jet}$	erg	$\rm L[10^{46}, 10^{53}]$	$\rm L(50.3^{+1.5}_{-2.0})$
ISM density	n_0	$\rm cm^{-3}$	$\rm L[10^{-5}, 10^2]$	$\rm L(-1.1^{+1.8}_{-1.9})$
Particle equipartition parameter	ϵ_e		$\rm L[10^{-5}, 1]$	$\rm L(-2.2^{+1.2}_{-1.5})$
Magnetic field equipartition parameter	ϵ_B		$\rm L[10^{-5}, 1]$	$\rm L(-2.8 \pm 1.3)$
Jet opening angle	θ_c	rad	0.1	
Electron spectral index	p		2.5	
Initial Lorentz factor	Γ_0		100	
Accelerated electron fraction	ξ_N		1	

Table A19. Priors and summary statistics for the joint radio and X-ray power-law synchrotron blast wave model in Fig. 6. Priors are either uniform (U) or log-uniform (L). The values shown for the posterior are the median and 1σ uncertainties. Posterior values denoted with L are given in log-space.

Parameter	Symbol	Units	Prior	Posterior
Shock velocity	$v_{\rm shock}$	$\rm km\ s^{-1}$	$\rm U[10^3, 3 \times 10^4]$	29996^{+3}_{-6}
CSM density at 10^{15} cm	A	$\rm cm^{-3}$	$\rm L[10^{-5}, 10^{15}]$	$\rm L(10.02^{+0.03}_{-0.02})$
CSM density index	s		U[0,4]	2.67 ± 0.01
Electron spectral index	p		U[2, 3]	$2.85^{+0.02}_{-0.01}$
Particle equipartition parameter	ϵ_e		$\rm L[10^{-5}, 1]$	$\rm L(-0.0010^{+0.0007}_{-0.0018})$
Magnetic field equipartition parameter	ϵ_B		$\rm L[10^{-5}, 1]$	$\rm L(-4.99 \pm 0.00)$

Downloaded from academic.oup.com/mnras/article/550/1/stag1104/8705434 by Sarah Dakin user on 15 September 2026

Table A20. Same as Table A19, but for the power-law synchrotron blast wave + gaussian jet afterglow model.

Parameter	Symbol	Units	Prior	Posterior
Observer angle	$\theta_{\rm obs}$	rad	Sine[0, $\pi/2$]	$0.610^{+0.049}_{-0.005}$
Isotropic equivalent jet energy	$E_{\rm jet}$	erg	L[10^{46}, 10^{53}]	L($50.78^{+0.05}_{-0.04}$)
ISM density	n_0	$\rm cm^{-3}$	L[10^{-5}, 10^{2}]	L($-0.62^{+0.16}_{-0.05}$)
Particle equipartition parameter (afterglow)	$\epsilon_{\rm e,GRB}$		L[10^{-5}, 1]	L($-0.028^{+0.16}_{-0.20}$)
Magnetic field equipartition parameter (afterglow)	$\epsilon_{\rm B,GRB}$		L[10^{-5}, 1]	L(-0.22 ± 0.11)
Shock velocity	$v_{\rm shock}$	$\rm km\ s^{-1}$	U[10^{3}, 3×10^{4}]	25000^{+3000}_{-4000}
CSM density at 10^{15} cm	A	$\rm cm^{-3}$	L[10^{-5}, 10^{15}]	L($8.6^{+0.6}_{-0.9}$)
CSM density index	s		U[0,4]	2.34 ± 0.00
Particle equipartition parameter (blast wave)	$\epsilon_{\rm e,ej}$		L[10^{-5}, 1]	L($-1.19^{+0.67}_{-0.90}$)
Magnetic field equipartition parameter (blast wave)	$\epsilon_{\rm B,ej}$		L[10^{-5}, 1]	L($-2.5^{+1.3}_{-0.9}$)
Jet core angle	θ_c	rad	0.1	
Jet edge angle	θ_j	rad	0.2	
Electron spectral index (afterglow)	$p_{\rm GRB}$		2.5	
Initial Lorentz factor	Γ_0		100	
Accelerated electron fraction	ξ_N		1	
Electron spectral index (blast wave)	$p_{\rm ej}$		2.5	

APPENDIX B: THE PHOTOSPHERE OF A HOMOLOGOUS EXPANDING MEDIUM

One argument against interpretations involving SNe, jets, or other expanding media is the behaviour of the photosphere of AT2024wpp. The photosphere peaks at ~ 5 d, but the spectra suggest that ejecta remains optically thick until $\gtrsim$40 d (D. A. Perley et al. 2026). The time-scale between when the photospheric radius peaks and when the ejecta becomes optically thin can be derived using a few simple assumptions and compared to the observed data.

Assume that the ejecta is expanding homologously with a power law density profile $\rho \propto v^{-\alpha}$, where $\alpha \geq 0$. The total mass of the ejecta is $M_{\rm ej}$ and the inner and outer edges of the ejecta are traveling at $v_{\rm in}$ and $v_{\rm out}$ respectively. The opacity κ is assumed to be constant and the ejecta is assumed to be spherical. The initial size of the object is initially assumed to be small, although we show the effect of relaxing that assumption after.

The photospheric radius $R_{\rm phot}$ can be derived by finding the location where the integrated optical depth from the edge of the ejecta becomes $\sim 2/3$ (W. D. Arnett 1980; W. D. Arnett & A. Fu 1989), i.e.

$$2/3 = \int_{R_{\rm phot}}^{v_{\rm out}t} \rho(r, t)\kappa\,{\rm d}r. \quad \text{(B1)}$$

Instead of continuing the derivation for arbitrary α, we instead focus on the two extreme cases, $\alpha = 0$ and $\alpha \rightarrow \infty$.

For $\alpha = 0$, the density is

$$\rho = \frac{3M_{\rm ej}}{4\pi(v_{\rm out}^3 - v_{\rm in}^3)t^3}. \quad \text{(B2)}$$

Substituting this into equation (B1) gives

$$2/3 = \int_{R_{\rm phot}}^{v_{\rm out}t} \frac{3M_{\rm ej}\kappa}{4\pi(v_{\rm out}^3 - v_{\rm in}^3)t^3}dr, \quad \text{(B3)}$$

$$= \frac{3M_{\rm ej}\kappa}{4\pi(v_{\rm out}^3 - v_{\rm in}^3)t^3}(v_{\rm out}t - R_{\rm phot}), \quad \text{(B4)}$$

$$R_{\rm phot} = v_{\rm out}t - \frac{8\pi(v_{\rm out}^3 - v_{\rm in}^3)t^3}{9M_{\rm ej}\kappa}. \quad \text{(B5)}$$

The time-scale for the photosphere to reach a peak is

$$t_{\rm phot,peak} = \sqrt{\frac{3M_{\rm ej}\kappa v_{\rm out}}{8\pi(v_{\rm out}^3 - v_{\rm in}^3)}}, \quad \text{(B6)}$$

and the time-scale when the entire ejecta becomes optically thin ($R_{\rm phot} = v_{\rm in}t$) and enters the nebular phase is

$$t_{\rm neb} = \sqrt{\frac{9M_{\rm ej}\kappa(v_{\rm out} - v_{\rm in})}{8\pi(v_{\rm out}^3 - v_{\rm in}^3)}}. \quad \text{(B7)}$$

The ratio between these two is

$$\frac{t_{\rm neb}}{t_{\rm phot,peak}} = \sqrt{\frac{3(v_{\rm out} - v_{\rm in})}{v_{\rm out}}} \leq \sqrt{3}. \quad \text{(B8)}$$

For $\alpha \rightarrow \infty$, the ejecta expands in a thin shell. $R_{\rm phot}$ will increases linearly until the ejecta becomes optically thin, so the ratio $t_{\rm neb}/t_{\rm phot,peak} \rightarrow 1$ for this case. Intermediate values of α should show $t_{\rm neb}/t_{\rm phot,peak}$ between 1 and $\sqrt{3}$, so the highest this ratio can go within the assumptions we have made is $\sqrt{3}$. Values higher than this indicate that the ejecta is likely highly non-spherical or not expanding homologously, either decelerating strongly, remaining stationary, or having mass continuously injected into the ejecta.

However, if the ejecta has an initial radius of R_0, then time t in equation (B5) gets replaced with $t + R_0/v_{\rm out}$, and both $t_{\rm phot,peak}$ and $t_{\rm neb}$ become smaller by $R_0/v_{\rm out}$, thus, the ratio between them becomes

$$\frac{t_{\rm neb}}{t_{\rm phot,peak}} = \frac{t_{\rm neb(R_0=0)} - R_0/v_{\rm out}}{t_{\rm phot,peak(R_0=0)} - R_0/v_{\rm out}} > \frac{t_{\rm neb(R_0=0)}}{t_{\rm phot,peak(R_0=0)}}. \quad \text{(B9)}$$

Thus, an extended progenitor on the order of $R_0 = v_{\rm out}t_{\rm phot,peak(R_0=0)}$ can have a high enough ratio to be consistent with observations. However, for AT 2024wpp, this radius is $\gtrsim 10^{15}$ cm, which rules out any known type of progenitor star.

This paper has been typeset from a TEX/LATEX file prepared by the author.

SO

© The Author(s) 2026.
Published by Oxford University Press on behalf of Royal Astronomical Society. This is an Open Access article distributed under the terms of the Creative Commons Attribution License (https://creativecommons.org/licenses/by/4.0/), which permits unrestricted reuse, distribution, and reproduction in any medium, provided the original work is properly cited.

Downloaded from academic.oup.com/mnras/article/550/1/stag1104/8705434 by Sarah Dakin user on 15 September 2026